



Controlling the fracture response of structures via topology optimization: From delaying fracture nucleation to maximizing toughness

Yingqi Jia^a, Oscar Lopez-Pamies^a, Xiaojia Shelly Zhang^{a,b,*}

^a Department of Civil and Environmental Engineering, University of Illinois at Urbana-Champaign, Urbana, IL 61801, USA

^b Department of Mechanical Science and Engineering, University of Illinois at Urbana-Champaign, Urbana, IL 61801, USA

ARTICLE INFO

Keywords:

Brittle fracture
Topology optimization
Strength
Overall toughness
toughening mechanism
Critical energy release rate

ABSTRACT

It is now a well-established fact that even simple topology variations can drastically change the fracture response of structures. With the objective of gaining quantitative insight into this phenomenon, this paper puts forth a density-based topology optimization framework for the fracture response of structures subjected to quasistatic mechanical loads. One of the two key features of the proposed framework is that it makes use of a complete phase-field fracture theory that has been recently shown capable of accurately describing the nucleation and propagation of brittle fracture in a wide range of nominally elastic materials under a wide range of loading conditions. The other key feature is that the framework is based on a multi-objective function that allows optimizing in a weighted manner: (i) the initial stiffness of the structure, (ii) the first instance at which fracture nucleates, and (iii) the energy dissipated by fracture propagation once fracture nucleation has occurred. The focus is on the basic case of structures made of a single homogeneous material featuring an isotropic linear elastic behavior alongside an isotropic strength surface and toughness. Novel interpolation rules are proposed for each of these three types of material properties. As a first effort to gain quantitative insight, the framework is deployed to optimize the fracture response of 2D structures wherein the fracture is bound to nucleate in three different types of regions: within the bulk, from geometric singularities (pre-existing cracks and sharp corners), and from smooth parts of the boundary. The obtained optimized structures are shown to exhibit significantly enhanced fracture behaviors compared to those of structures that are optimized according to conventional stiffness maximization. Furthermore, the results serve to reveal a variety of strengthening and toughening mechanisms. These include the promotion of highly porous structures, the formation of tension-compression asymmetric regions, and the removal of cracks and sharp corners. The particular mechanism that is preferred by a given structure, not surprisingly, correlates directly to the elastic, strength, and toughness properties of the material that is made of.

1. Introduction

Due to its overwhelming pervasiveness, the understanding of fracture in solid matter is a fundamental problem in mechanics that has had a long and rich history. By the same token, it has long been plain that having the ability to control/design the fracture

* Correspondence to: Department of Civil and Environmental Engineering, University of Illinois at Urbana-Champaign, 205 North Mathews Ave, Urbana, IL 61801, USA.

E-mail addresses: yingqij2@illinois.edu (Y. Jia), pamies@illinois.edu (O. Lopez-Pamies), zhangxs@illinois.edu (X.S. Zhang).

<https://doi.org/10.1016/j.jmps.2023.105227>

Received 16 October 2022; Received in revised form 20 January 2023; Accepted 22 January 2023

Available online 30 January 2023

0022-5096/© 2023 Elsevier Ltd. All rights reserved.

behavior of materials and structures could drastically improve their performance and also possibly enable new technologies. Over the past few decades, strides have been made towards achieving such control, primarily by identifying microscopic mechanisms that lead to enhanced toughening behaviors, see, e.g., Gao and Rice (1989), Bower and Ortiz (1991), Huang and Kinloch (1992), Chen et al. (2010), Mirkhalaf et al. (2018), Jia et al. (2020), Ritchie (2021), Brodnik et al. (2021) and Michel and Suquet (2022). Among these, it is instructive to single out the experimental studies in Huang and Kinloch (1992) and Brodnik et al. (2021), where the mere presence of suitably distributed pores in otherwise homogeneous materials was shown to lead to significant enhancements of the apparent toughness. They are clear examples of the profound effects that simple topological variations can have on the fracture response of structures. In spite of this realization, a systematic study — beyond intuitive guessing — of optimal topologies has been out of reach because of the lack of a complete quantitative description of when and how cracks nucleate and propagate in a given structure under arbitrary loading conditions.

In this context, a series of recent papers (Kumar et al., 2018b; Kumar and Lopez-Pamies, 2020; Kumar et al., 2020; Kumar and Lopez-Pamies, 2021; Kumar et al., 2022) have provided a wide range of validation results for a broad spectrum of materials (silicone, titania, graphite, polyurethane, PMMA, alumina, natural rubber, glass) and an equally broad spectrum of specimen geometries (with large and small pre-existing cracks, V notches, U notches, and smooth boundaries) and loading conditions suggesting that the phase-field fracture theory initiated by Kumar et al. (2018a) may indeed provide a complete framework for the description of fracture nucleation and propagation in nominally elastic brittle materials when subjected to arbitrary quasistatic deformations. In a nutshell, the theory of Kumar et al. (2018a) corresponds to a generalization of the classical phase-field regularization (Bourdin et al., 2000) of the variational theory of brittle fracture of Francfort and Marigo (1998), which in turn corresponds to the mathematical statement of Griffith's fracture postulate in its general form of energy cost–benefit analysis (Griffith, 1921). The generalization amounts: (i) to considering the Euler–Lagrange equations of the classical phase-field regularization — and not the variational principle itself — as the primal model and (ii) to adding an external driving force in the Euler–Lagrange equation governing the evolution of the phase field to describe the macroscopic manifestation of the presence of the inherent defects in the material, that is, its strength at large. Having the complete formulation of fracture (Kumar et al., 2018a) at our disposal, we are now in a position to study systematically the topology optimization of the fracture response of structures under arbitrary quasistatic mechanical loads. This is precisely the objective of this work. To do so, we put forth a density-based topology optimization framework. The focus is on structures made of a single homogeneous isotropic linear elastic material, whose strength surface and toughness are also isotropic. The framework introduces a multi-objective function that allows optimizing in a weighted manner of choice:

- the initial stiffness of the structure,
- the first instance at which fracture nucleates, and
- the energy dissipated by fracture propagation once fracture nucleation has occurred.

This generalizes conventional topology optimization approaches, which have traditionally targeted the maximization of the stiffness of structures under the premise that materials remain always elastic and, in particular, that they never fracture (Bendsoe and Kikuchi, 1988; Allaire, 2002; Bendsoe and Sigmund, 2003; Wang et al., 2021; Li et al., 2022).

The paper is organized as follows. We begin in Section 2 by briefly summarizing the specialization (Kumar et al., 2020) of the general fracture theory (Kumar et al., 2018a) to the linear elastic materials of interest in this work. We present the density-based topology optimization framework *per se* in Section 3. In Section 4, we deploy the proposed topology optimization framework to generate representative results. Precisely, we present four numerical examples that serve to illustrate the various competitions that can take place between the topology of a structure and the elastic, strength, and toughness properties of the material that is made of. Fig. 1 provides a schematic summary of the optimization framework proposed in Section 3 and of a representative result from Section 4. It illustrates that the design domain may contain pre-existing cracks, sharp or rounded corners, as well as smooth boundaries. Given a set of boundary conditions, under the constraint of a given total usage of material, the framework seeks to optimize the fracture response of the structure by delaying the first instance at which fracture nucleates while maintaining a sufficiently large initial stiffness and maximizing the energy dissipated by fracture propagation once the fracture has occurred. These three objectives are manifest in part (b) of Fig. 1, where the force–displacement curve obtained by the proposed framework is compared to that obtained from conventional stiffness maximization for one of the four examples considered in Section 4. Notably, at the expense of a mild decrease in initial stiffness, the result shows that fracture first nucleates in the new design at a significantly (about 100%) larger applied load than in the conventional design. What is more, the total work required to lead to the complete failure of the structure in the new design is also significantly (about 271%) larger. We conclude this work by making a number of final comments in Section 5. The paper is complemented by three appendices. Appendix A presents the derivation of the scaling function proposed in the interpolation scheme. Appendix B provides details on the sensitivity analysis and convergence histories. Appendix C presents two investigations on finite element meshes.

A comment on other topology optimization frameworks accounting for fracture. Before proceeding with the bulk of the paper, it is appropriate to acknowledge the flurry of studies that have just recently appeared in the literature on the topology optimization of structures that do account for fracture properties (Da et al., 2018; Xia et al., 2018; Russ and Waisman, 2019; Da and Qian, 2020; Da and Yvonnet, 2020; Russ and Waisman, 2020; Wu et al., 2020; Li et al., 2021; Wu et al., 2021; Da et al., 2022; Da and Chen, 2022; Desai et al., 2022; Wu et al., 2022; Zhang et al., 2022).

Invariably, all of these studies employ the classical phase-field fracture theory (Bourdin et al., 2000), or some variation of it (Miehe et al., 2010; Tanné et al., 2018), to describe fracture. Due to their use of the classical phase-field theory, the designs generated by these formulations are not fully optimal in their fracture response. This is because the accurate description of fracture

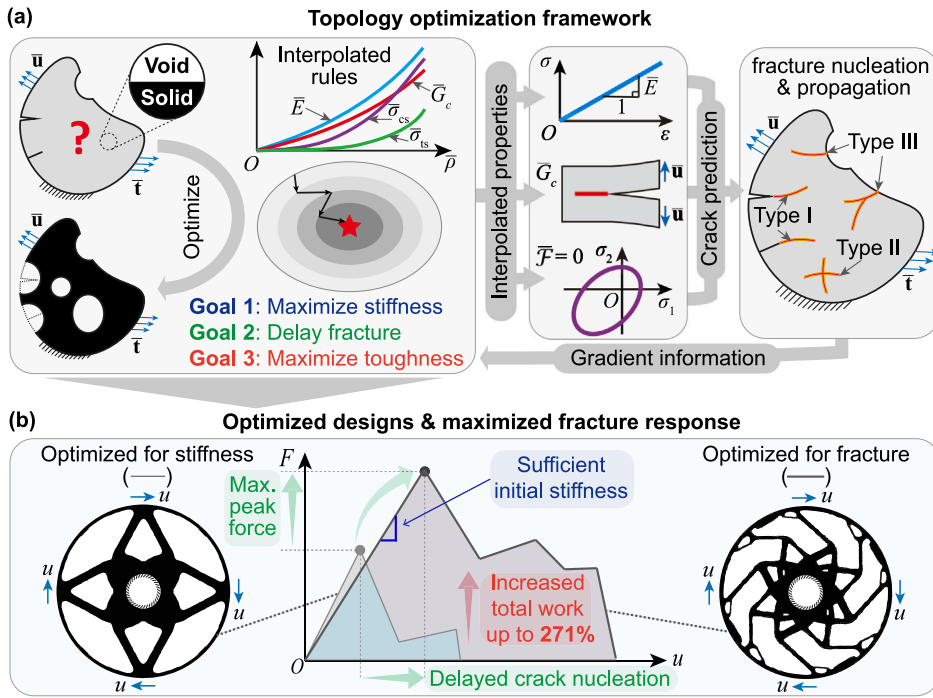


Fig. 1. (a) Schematic of the proposed topology optimization framework to optimize the fracture response of structures made of a single homogeneous material with isotropic linear elastic, strength, and toughness properties. (b) Comparison of the fracture response of a structure optimized with the proposed framework and that of a structure optimized by the conventional stiffness maximization.

nucleation is paramount in a topology optimization process, yet, as elaborated at length in Kumar et al. (2020), the classical phase-field theory (Bourdin et al., 2000) cannot describe nucleation of fracture in general as it does not account for the strength of the material as one of its three basic ingredients, the other two being the elasticity and the toughness.

To see that an accurate description of fracture nucleation — and not just of fracture propagation — is paramount in a topology optimization process consider the following scenario. Irrespectively of whether a structure contains a pre-existing crack in its initial configuration, it may be that at a later time in the optimization process, the structure contains holes with sharp or smooth boundaries (as illustrated in Section 4 below, the latter is actually often the case). Fracture nucleation in such a configuration is governed either by the strength or by mediation between the strength and the toughness of the material. Consequently, any further iterations in the optimization process necessarily require an accurate description of fracture nucleation from all possible regions in the structure, within the bulk, from geometric singularities, and from smooth parts of the boundary.

2. The phase-field fracture theory

2.1. The three basic constitutive ingredients for a complete theory of fracture nucleation and propagation

When viewed collectively, as discussed at length in Kumar and Lopez-Pamies (2020) and Kumar et al. (2020), the vast macroscopic experimental observations that have been accumulated since the early 1900s on the fracture behavior of a wide range of ceramics, metals, and polymers alike provide a complete — albeit partly qualitative — picture of how fracture nucleate and propagate in nominally elastic brittle materials when subjected to mechanical loads that are applied quasistatically. In sum, *nucleation of fracture*

- in the bulk of an elastic brittle material (under uniform states of stress) is governed by its strength,
- from large pre-existing cracks is governed by the Griffith competition between its elastic energy and fracture energy,
- from boundary points, be them smooth or sharp, and small pre-existing cracks is governed by the interaction among its strength, elastic energy, and fracture energy,

while *propagation of fracture*

- is, much like nucleation from large pre-existing cracks, also governed by the Griffith competition between the elastic and fracture energies of the material.

It follows, that any formulation that aims at providing a complete macroscopic theory of nucleation and propagation of fracture in elastic brittle materials must account for three basic constitutive ingredients:

- (i) the elasticity of the material,
- (ii) its strength, and
- (iii) its critical energy release rate.

Remark 1. The ingredient of strength here merits explicit clarification. It refers to the general definition of strength introduced in Kumar and Lopez-Pamies (2020) and Kumar et al. (2020), which we recall here for the reader’s convenience. When any piece of the elastic brittle material of interest is subjected to a state of monotonically increasing uniform but otherwise arbitrary stress, the fracture will nucleate from one or more of its inherent defects at a critical value of the applied stress. The set of all such critical stresses defines a surface in stress space. In terms of the Cauchy stress tensor σ , we write $\mathcal{F}(\sigma) = 0$. This definition generalizes the various notions of “tensile” and “shear” strengths that were proposed on the heels of the introduction of the stress tensor (Cauchy, 1823) by numerous pioneers of continuum mechanics including Lamé, Clapeyron, Tresca, and Mohr; see, e.g., the historical account on the rupture of solids in the classic monograph by Love (1906, Section 83).

2.2. The basic case of isotropic linear elastic materials with isotropic strength and toughness

As announced in the Introduction, the focus of this work is on structures that are made of a single homogeneous material featuring an isotropic linear elastic behavior alongside an isotropic strength surface and toughness. Accordingly, the three basic ingredients of elasticity, strength, and toughness are described by the stored-energy function

$$W(\mathbf{E}) = \mu \operatorname{tr} \mathbf{E}^2 + \frac{\lambda}{2} (\operatorname{tr} \mathbf{E})^2, \tag{1}$$

an isotropic strength surface

$$\mathcal{F}(\sigma_1, \sigma_2, \sigma_3) = 0,$$

and the constant critical energy release rate

$$G_c. \tag{2}$$

In these expressions, λ and μ stand for the first and second Lamé moduli of the material, $\mathbf{E} = \frac{1}{2}(\nabla \mathbf{u} + \nabla \mathbf{u}^T)$ is the infinitesimal strain tensor, \mathbf{u} is the displacement field, and $\sigma_1, \sigma_2, \sigma_3$ denote the Cauchy principal stresses.

In practice, routine experiments suffice to measure the Lamé moduli λ and μ and the critical energy release rate G_c of a given material of interest. By contrast, it is difficult to measure its entire strength surface $\mathcal{F}(\sigma_1, \sigma_2, \sigma_3)$. In fact, only the uniaxial tensile and compressive strengths of materials are typically available in the literature. To deal with this lack of experimental results, one usually resorts to the use of a model that can fit and extrapolate the available strength data to the entire stress space. For definiteness, throughout this work, we make use of the Drucker–Prager strength surface

$$\mathcal{F}(\sigma_1, \sigma_2, \sigma_3) = \sqrt{J_2} + \frac{\sigma_{cs} - \sigma_{ts}}{\sqrt{3}(\sigma_{cs} + \sigma_{ts})} I_1 - \frac{2\sigma_{cs}\sigma_{ts}}{\sqrt{3}(\sigma_{cs} + \sigma_{ts})} = 0, \tag{3}$$

where

$$I_1 = \operatorname{tr} \sigma = \sigma_1 + \sigma_2 + \sigma_3, \quad J_2 = \frac{1}{2} \operatorname{tr} \sigma_D^2 = \frac{1}{6} ((\sigma_1 - \sigma_2)^2 + (\sigma_1 - \sigma_3)^2 + (\sigma_2 - \sigma_3)^2),$$

with $\sigma_D = \sigma - 1/3 (\operatorname{tr} \sigma) \mathbf{I}$, and where σ_{ts} and σ_{cs} are the uniaxial tensile and compressive strengths. The two-material-parameter strength surface (3) was originally introduced by Drucker and Prager (Drucker and Prager, 1952) to model the yielding of soils. As comparisons with experiments have later demonstrated, it is a surface that is capable of describing reasonably well the strength of many nominally brittle materials; see Chapter 10 in Munz and Fett (1999) and Section 2 in Kumar et al. (2020).

2.3. The governing equations

Consider a structure made of an isotropic linear elastic brittle material, with stored-energy function (1), strength surface (3), and critical energy release rate (2), that occupies an open bounded domain $\Omega \subset \mathbb{R}^3$, with boundary $\partial\Omega$ and unit outward normal \mathbf{N} , in its undeformed and stress-free configuration at time $t = 0$. At a later time $t \in (0, T]$, due to an externally applied displacement $\bar{\mathbf{u}}(\mathbf{X}, t)$ on a part $\partial\Omega_D$ of the boundary and a traction $\bar{\mathbf{t}}(\mathbf{X}, t)$ on the complementary part $\partial\Omega_{\mathcal{N}} = \partial\Omega \setminus \partial\Omega_D$, the position vector \mathbf{X} of a material point moves to a new position specified by

$$\mathbf{x} = \mathbf{X} + \mathbf{u}(\mathbf{X}, t)$$

in terms of the displacement field \mathbf{u} . In addition to the above-described deformation, the externally applied mechanical stimuli may also result in the nucleation and subsequent propagation of cracks in the material. We describe those in a regularized fashion via an order parameter or phase field

$$v = v(\mathbf{X}, t)$$

taking values in the range $[0, 1]$. Precisely, the value $v = 1$ identifies the sound regions of the material and $v = 0$ those that have been fractured, while the transition from $v = 1$ to $v = 0$ is set to occur smoothly over regions of small thickness of regularization length scale $\epsilon > 0$.

According to the theory in Kumar et al. (2020), the displacement field $\mathbf{u}(\mathbf{X}, t)$ and phase field $v(\mathbf{X}, t)$ at any material point $\mathbf{X} \in \bar{\Omega} = \Omega \cup \partial\Omega$ and time $t \in [0, T]$ are determined by the system of coupled partial differential equations (PDEs)

$$\begin{cases} \text{Div} \left[v^2 \frac{\partial W}{\partial \mathbf{E}}(\mathbf{E}(\mathbf{u})) \right] = \mathbf{0}, & (\mathbf{X}, t) \in \Omega \times [0, T], \\ \mathbf{u} = \bar{\mathbf{u}}(\mathbf{X}, t), & (\mathbf{X}, t) \in \partial\Omega_D \times [0, T], \\ \left[v^2 \frac{\partial W}{\partial \mathbf{E}}(\mathbf{E}(\mathbf{u})) \right] \mathbf{N} = \bar{\mathbf{t}}(\mathbf{X}, t), & (\mathbf{X}, t) \in \partial\Omega_N \times [0, T] \end{cases} \quad (4)$$

and

$$\begin{cases} \text{Div} \left[\epsilon G_c \nabla v \right] = \frac{8}{3} v W(\mathbf{E}(\mathbf{u})) - \frac{4}{3} c_e(\mathbf{X}, t) - \frac{G_c}{2\epsilon}, & \text{if } \dot{v}(\mathbf{X}, t) < 0, \quad (\mathbf{X}, t) \in \Omega \times [0, T] \\ \text{Div} \left[\epsilon G_c \nabla v \right] \geq \frac{8}{3} v W(\mathbf{E}(\mathbf{u})) - \frac{4}{3} c_e(\mathbf{X}, t) - \frac{G_c}{2\epsilon}, & \text{if } v(\mathbf{X}, t) = 1 \text{ or } \dot{v}(\mathbf{X}, t) > 0, \quad (\mathbf{X}, t) \in \Omega \times [0, T] \\ \text{Div} \left[\epsilon G_c \nabla v \right] \leq \frac{8}{3} v W(\mathbf{E}(\mathbf{u})) - \frac{4}{3} c_e(\mathbf{X}, t) - \frac{G_c}{2\epsilon}, & \text{if } v(\mathbf{X}, t) = 0, \quad (\mathbf{X}, t) \in \Omega \times [0, T] \\ \nabla v \cdot \mathbf{N} = 0, & (\mathbf{X}, t) \in \partial\Omega \times [0, T] \end{cases} \quad (5)$$

with $\mathbf{u}(\mathbf{X}, 0) \equiv \mathbf{0}$ and $v(\mathbf{X}, 0) \equiv 1$, where $c_e(\mathbf{X}, t)$ is a driving force whose specific constitutive prescription depends on the particular form of strength surface. For the Drucker–Prager strength surface (3), we make use of one of the prescriptions provided in Kumar et al. (2022). It reads

$$c_e(\mathbf{X}, t) = \beta_2^\epsilon \sqrt{J_2} + \beta_1^\epsilon I_1 + \beta_0^\epsilon,$$

where I_1 and J_2 are the invariants

$$I_1 = \text{tr } \boldsymbol{\sigma} = (3\lambda + 2\mu)v^2 \text{tr } \mathbf{E}(\mathbf{u}), \quad J_2 = \frac{1}{2} \text{tr } \boldsymbol{\sigma}_D^2 = 2\mu^2 v^4 \text{tr } \mathbf{E}_D^2(\mathbf{u}) \quad \text{with} \quad \mathbf{E}_D = \mathbf{E} - \frac{1}{3} (\text{tr } \mathbf{E}) \mathbf{I}$$

of the Cauchy stress tensor

$$\boldsymbol{\sigma}(\mathbf{X}, t) = v^2 \frac{\partial W}{\partial \mathbf{E}}(\mathbf{E}(\mathbf{u})),$$

while $\beta_0^\epsilon, \beta_1^\epsilon, \beta_2^\epsilon$ are the ϵ -dependent coefficients

$$\begin{cases} \beta_0^\epsilon = \delta^\epsilon \frac{3G_c}{8\epsilon} \\ \beta_1^\epsilon = - \left(\frac{(1 + \delta^\epsilon)(\sigma_{cs} - \sigma_{ts})}{2\sigma_{cs}\sigma_{ts}} \right) \frac{3G_c}{8\epsilon} + \frac{\sigma_{ts}}{6(3\lambda + 2\mu)} + \frac{\sigma_{ts}}{6\mu} \\ \beta_2^\epsilon = - \left(\frac{\sqrt{3}(1 + \delta^\epsilon)(\sigma_{cs} + \sigma_{ts})}{2\sigma_{cs}\sigma_{ts}} \right) \frac{3G_c}{8\epsilon} + \frac{\sigma_{ts}}{2\sqrt{3}(3\lambda + 2\mu)} + \frac{\sigma_{ts}}{2\sqrt{3}\mu} \end{cases} .$$

In these last expressions, δ^ϵ is a dimensionless ϵ -dependent parameter whose calibration needs to be carried out by following the procedure laid out in Section 4.3.2 of Kumar et al. (2020).

Remark 2. The regularization length ϵ in Eqs. (4)–(5) is just a regularization parameter that is void of any further physical meaning. In practice, it should be selected to be smaller than the smallest characteristic length scale in the structural problem at hand.

Remark 3. On their own, Eqs. (4) and (5) are second-order elliptic PDEs for the displacement field \mathbf{u} and the phase field v . Accordingly, their numerical solution is amenable to a standard finite-element (FE) staggered scheme in which (4) and (5) are discretized with finite elements and solved iteratively one after the other until convergence is reached. A FEniCS implementation of such a scheme¹ is available in GitHub.

3. The proposed topology optimization framework

In this section, we introduce a density-based topology optimization framework built on the phase-field fracture theory (4)–(5) that is aimed at optimizing the fracture response of structures subjected to quasistatic mechanical loading. We begin in Sections 3.1 and 3.2 by introducing the design parameterization and associated interpolations for all three types of material — elastic, strength, and toughness — properties. In Section 3.3, we present the multi-objective topology optimization theory that defines the optimal fracture response of structures. Finally, in Section 3.4, we describe the numerical implementation to solve the resulting optimization problem.

¹ https://github.com/adityakr42/FEniCS_Fracture_Kumar_Lopez-Pamies

3.1. Design parameterization

In a given design domain Ω , density-based topology optimization introduces a dimensionless continuous scalar field $\rho(\mathbf{X}) \in [0, 1]$, referred to as the design variable, in terms of which the physical density field $\bar{\rho}(\mathbf{X}) \in [0, 1]$ that parameterizes the topological space is defined (Bendsoe and Sigmund, 2003). For well-known computational reasons (to reduce space-discretization dependencies, to eliminate checker-board patterns, and to also enhance the discreteness of final designs, i.e., to ensure the 0–1 solution), we define the latter in terms of the former by the relation

$$\bar{\rho}(\mathbf{X}) = \frac{\tanh(\beta\theta) + \tanh(\beta(\bar{\rho}(\mathbf{X}) - \theta))}{\tanh(\beta\theta) + \tanh(\beta(1 - \theta))}, \tag{6}$$

where

$$\bar{\rho}(\mathbf{X}) = \frac{\int_{\Omega} w(\mathbf{X}, \mathbf{X}')\rho(\mathbf{X}') d\mathbf{X}'}{\int_{\Omega} w(\mathbf{X}, \mathbf{X}') d\mathbf{X}'}. \tag{7}$$

In these expressions, β is the sharpness parameter, $\theta = 0.5$ is the projection threshold value, and the coefficient $w(\mathbf{X}, \mathbf{X}') = \max\{0, R - |\mathbf{X} - \mathbf{X}'|\}$ is a weighting factor determined by the filter radius R and the Euclidean distance between material points \mathbf{X} and \mathbf{X}' (Bourdin, 2001).

Following the standard convention, the value $\bar{\rho} = 0$ represents a void, the value $\bar{\rho} = 1$ represents the solid (physical material), while the intermediate values $0 < \bar{\rho} < 1$ describe an interpolated material. In terms of this parameterization, we write the stored-energy function in a given design domain Ω as $\bar{W}(\mathbf{E}(\mathbf{u}); \bar{\rho})$, the tensile and compressive strengths as $\bar{\sigma}_{ts}(\bar{\rho})$ and $\bar{\sigma}_{cs}(\bar{\rho})$, the critical energy release rate as $\bar{G}_c(\bar{\rho})$, and the dimensionless parameter as $\bar{\delta}^\epsilon(\bar{\rho})$. In a similar fashion, we write the corresponding displacement and phase fields as $\mathbf{u}(\mathbf{X}, t; \bar{\rho})$ and $v(\mathbf{X}, t; \bar{\rho})$.

The parameterized phase-field equations. Given the above-defined parameterization, the phase-field fracture equations (4)–(5) need to be generalized to describe a material system with spatially heterogeneous elastic, strength, and toughness properties, as characterized by the physical density variable $\bar{\rho}(\mathbf{X})$. This raises the question of whether additional “interfacial” strength and toughness should be accounted for at material discontinuities. Since the focus here is on structures made of a single homogeneous material that may contain voids, it is sensible to discard the presence of such additional “interfacial” properties. The relevant parameterized phase-field equations are then simply obtained by augmenting the fields in (4)–(5) with their dependence on $\bar{\rho}(\mathbf{X})$. We thus have

$$\begin{cases} \text{Div} \left[v^2 \frac{\partial \bar{W}}{\partial \mathbf{E}}(\mathbf{E}(\mathbf{u}); \bar{\rho}) \right] = \mathbf{0}, & (\mathbf{X}, t) \in \Omega \times [0, T], \\ \mathbf{u} = \bar{\mathbf{u}}(\mathbf{X}, t), & (\mathbf{X}, t) \in \partial\Omega_D \times [0, T], \\ \left[v^2 \frac{\partial \bar{W}}{\partial \mathbf{E}}(\mathbf{E}(\mathbf{u}); \bar{\rho}) \right] \mathbf{N} = \bar{\mathbf{t}}(\mathbf{X}, t), & (\mathbf{X}, t) \in \partial\Omega_N \times [0, T] \end{cases} \tag{8}$$

and

$$\begin{cases} \text{Div} \left[\epsilon \bar{G}_c(\bar{\rho}) \nabla v \right] = \frac{8}{3} v \bar{W}(\mathbf{E}(\mathbf{u}); \bar{\rho}) - \frac{4}{3} c_e(\mathbf{X}, t; \bar{\rho}) - \frac{\bar{G}_c(\bar{\rho})}{2\epsilon}, & \text{if } \dot{v}(\mathbf{X}, t; \bar{\rho}) < 0, \quad (\mathbf{X}, t) \in \Omega \times [0, T] \\ \text{Div} \left[\epsilon \bar{G}_c(\bar{\rho}) \nabla v \right] \geq \frac{8}{3} v \bar{W}(\mathbf{E}(\mathbf{u}); \bar{\rho}) - \frac{4}{3} c_e(\mathbf{X}, t; \bar{\rho}) - \frac{\bar{G}_c(\bar{\rho})}{2\epsilon}, & \text{if } v(\mathbf{X}, t; \bar{\rho}) = 1 \text{ or } \dot{v}(\mathbf{X}, t; \bar{\rho}) > 0, \quad (\mathbf{X}, t) \in \Omega \times [0, T] \\ \text{Div} \left[\epsilon \bar{G}_c(\bar{\rho}) \nabla v \right] \leq \frac{8}{3} v \bar{W}(\mathbf{E}(\mathbf{u}); \bar{\rho}) - \frac{4}{3} c_e(\mathbf{X}, t; \bar{\rho}) - \frac{\bar{G}_c(\bar{\rho})}{2\epsilon}, & \text{if } v(\mathbf{X}, t; \bar{\rho}) = 0, \quad (\mathbf{X}, t) \in \Omega \times [0, T] \\ \nabla v \cdot \mathbf{N} = 0, & (\mathbf{X}, t) \in \partial\Omega \times [0, T] \end{cases} \tag{9}$$

with

$$\begin{aligned} c_e(\mathbf{X}, t; \bar{\rho}) = & \left(- \left(\frac{\sqrt{3}(1 + \bar{\delta}^\epsilon(\bar{\rho}))(\bar{\sigma}_{cs}(\bar{\rho}) + \bar{\sigma}_{ts}(\bar{\rho}))}{2\bar{\sigma}_{cs}(\bar{\rho})\bar{\sigma}_{ts}(\bar{\rho})} \right) \frac{3\bar{G}_c(\bar{\rho})}{8\epsilon} + \frac{\sqrt{3}\bar{\sigma}_{ts}(\bar{\rho})}{2\bar{E}(\bar{\rho})} \right) \frac{v^2 \bar{E}(\bar{\rho})}{1 + \bar{v}(\bar{\rho})} \sqrt{\frac{1}{2} \text{tr} \left(\mathbf{E}(\mathbf{u}) - \frac{1}{3} (\text{tr} \mathbf{E}(\mathbf{u})) \mathbf{I} \right)^2} + \\ & \left(- \left(\frac{(1 + \bar{\delta}^\epsilon(\bar{\rho}))(\bar{\sigma}_{cs}(\bar{\rho}) - \bar{\sigma}_{ts}(\bar{\rho}))}{2\bar{\sigma}_{cs}(\bar{\rho})\bar{\sigma}_{ts}(\bar{\rho})} \right) \frac{3\bar{G}_c(\bar{\rho})}{8\epsilon} + \frac{\bar{\sigma}_{ts}(\bar{\rho})}{2\bar{E}(\bar{\rho})} \right) \frac{v^2 \bar{E}(\bar{\rho})}{1 - 2\bar{v}(\bar{\rho})} \text{tr} \mathbf{E}(\mathbf{u}) + \bar{\delta}^\epsilon(\bar{\rho}) \frac{3\bar{G}_c(\bar{\rho})}{8\epsilon}, \end{aligned} \tag{10}$$

where, for consistency with the topology optimization literature, we have favored the use of the Young’s modulus and Poisson’s ratio

$$\bar{E}(\bar{\rho}) = \frac{\bar{\mu}(\bar{\rho}) \left(3\bar{\lambda}(\bar{\rho}) + 2\bar{\mu}(\bar{\rho}) \right)}{\bar{\lambda}(\bar{\rho}) + \bar{\mu}(\bar{\rho})} \quad \text{and} \quad \bar{v}(\bar{\rho}) = \frac{\bar{\lambda}(\bar{\rho})}{2(\bar{\lambda}(\bar{\rho}) + \bar{\mu}(\bar{\rho}))}$$

instead of the Lamé moduli as the elastic material constants.

3.2. Proposed interpolation rules for the material constants

Having identified (8)–(9) as the equations governing deformation and fracture in the design domain, the next step is to specify appropriate interpolation rules for all the underlying material properties: $\bar{E}(\bar{\rho})$, $\bar{\nu}(\bar{\rho})$, $\bar{\sigma}_{ts}(\bar{\rho})$, $\bar{\sigma}_{cs}(\bar{\rho})$, $\bar{G}_c(\bar{\rho})$, and $\bar{\delta}^{\epsilon}(\bar{\rho})$.

3.2.1. Elastic constants

For the Young’s modulus $\bar{E}(\bar{\rho})$ in the design domain, we make use of the interpolation rule

$$\bar{E}(\bar{\rho}) = \frac{1}{\sqrt{s(\bar{\rho})}} (\eta_E + (1 - \eta_E)\bar{\rho}^{p_E}) E, \tag{11}$$

which is a modification of the commonly used SIMP rule (Bendsøe and Sigmund, 1999). Here, we recall that E is the Young’s modulus of the actual material, $s(\bar{\rho})$ is a proposed strictly positive scaling function with extremal values $s(0) = s(1) = 1$ to be specified further below, η_E is a small positive number that serves to regularize the vanishingly small stiffness of the voids (ersatz material) in the design, and p_E is a positive number typically chosen such that $p_E \geq 3$.

For the Poisson’s ratio $\bar{\nu}(\bar{\rho})$, we make use of the conventional choice that its value is the same as that of the actual material for any $\bar{\rho}$, to wit,

$$\bar{\nu}(\bar{\rho}) = \nu. \tag{12}$$

3.2.2. Strength constants

For the tensile and compressive strengths $\bar{\sigma}_{ts}(\bar{\rho})$ and $\bar{\sigma}_{cs}(\bar{\rho})$ in the design domain, we select the SIMP rule

$$\begin{cases} \bar{\sigma}_{ts}(\bar{\rho}) = (\eta_{\sigma_{ts}} + (1 - \eta_{\sigma_{ts}})\bar{\rho}^{p_{\sigma}}) \sigma_{ts} \\ \bar{\sigma}_{cs}(\bar{\rho}) = (\eta_{\sigma_{cs}} + (1 - \eta_{\sigma_{cs}})\bar{\rho}^{p_{\sigma}}) \sigma_{cs} \end{cases}, \tag{13}$$

where $\eta_{\sigma_{ts}}$ and $\eta_{\sigma_{cs}}$ stand for two sufficiently small positive numbers that serve to regularize the vanishingly small strength of the voids in the design, the penalty parameter p_{σ} is a positive number typically chosen such that $p_{\sigma} \geq 1$, and where we recall that σ_{ts} and σ_{cs} are the tensile and compressive strengths of the actual material.

Remark 4. In regions where the density $\bar{\rho} \searrow 0$, fracture may nucleate because of their very small strength. To avoid this artificial behavior, it suffices to choose a smaller penalty parameter in (13) than in (11), that is,

$$p_{\sigma} < p_E.$$

3.2.3. Toughness

Similar to our proposed revised interpolation rule (11) for the Young’s modulus, we interpolate the critical energy release rate in the design domain as

$$\bar{G}_c(\bar{\rho}) = \frac{1}{\sqrt{s(\bar{\rho})}} (\eta_{G_c} + (1 - \eta_{G_c})\bar{\rho}^{p_{G_c}}) G_c, \tag{14}$$

where we recall that G_c denotes the critical energy release rate of the actual material. Accordingly, in this expression, η_{G_c} is a small positive number that serves to regularize the vanishingly small toughness of the voids in the design, the power p_{G_c} is a penalty parameter to be chosen such that $p_{G_c} \geq 1$, and $s(\bar{\rho})$ is the same strictly positive scaling function with $s(0) = s(1) = 1$ proposed in (11), which we are now ready to specify.

The choice of scaling function $s(\bar{\rho})$, regularization parameters η_E , $\eta_{\sigma_{ts}}$, η_{G_c} , and penalty parameters p_E , p_{σ} , p_{G_c} . Owing to the different units of the elastic ($force/length^2$), strength ($force/length^2$), and toughness properties ($force/length$), the Eqs. (8)–(9) feature an inherent set of characteristic length scales. Since the focus here is, again, on structures made of a single homogeneous material that may contain voids, it is reasonable to enforce that such a set of characteristic length scales remain the same in the design domain irrespective of the value of the density $\bar{\rho}$. We accomplish this by setting the scaling function $s(\bar{\rho})$ in (11) and (14) as

$$s(\bar{\rho}) = \frac{(\eta_E + (1 - \eta_E)\bar{\rho}^{p_E}) (\eta_{G_c} + (1 - \eta_{G_c})\bar{\rho}^{p_{G_c}})}{(\eta_{\sigma_{ts}} + (1 - \eta_{\sigma_{ts}})\bar{\rho}^{p_{\sigma}})^2}.$$

Given this choice, the requirement that $s(0) = s(1) = 1$ then implies that the parameters η_E , $\eta_{\sigma_{ts}}$, η_{G_c} must be chosen subject to the constraint

$$\eta_E \eta_{G_c} = \eta_{\sigma_{ts}}^2. \tag{15}$$

Now, the scaling function $s(\bar{\rho})$ should be selected to make (11) and (14) deviate as little as possible from the SIMP rule. This implies that the penalty parameters p_E , p_{σ} , p_{G_c} must be chosen subject to the constraint

$$p_E + p_{G_c} = 2p_{\sigma}. \tag{16}$$

The derivation of the scaling function $s(\bar{\rho})$ is detailed in Appendix A.

Table 1
Interpolation rules for all material constants entering the phase-field fracture equations (8)–(9).

Material constants	interpolation rules
Young's modulus $\bar{E}(\bar{\rho})$	revised SIMP rule (11)
Poisson's ratio $\bar{\nu}(\bar{\rho})$	constant (12)
Tensile strength $\bar{\sigma}_{ts}(\bar{\rho})$	SIMP rule (13) ₁
Compressive strength $\bar{\sigma}_{cs}(\bar{\rho})$	SIMP rule (13) ₂
Critical energy release rate $\bar{G}_c(\bar{\rho})$	revised SIMP rule (14)
Dimensionless parameter $\bar{\delta}^\varepsilon(\bar{\rho})$	fitting formula (17)

3.2.4. The dimensionless parameter $\bar{\delta}^\varepsilon(\bar{\rho})$

As remarked in the calibration process laid out in Section 4.3.2 of Kumar et al. (2020), the dimensionless parameter $\bar{\delta}^\varepsilon(\bar{\rho})$ in the driving force (10) takes on different values depending on the given elastic (\bar{E} and $\bar{\nu}$ here), strength ($\bar{\sigma}_{ts}$ and $\bar{\sigma}_{cs}$), and toughness (\bar{G}_c) constants of the material, as well as on the value of the regularization length ε used in the calculations. In principle, for the problem at hand, this means that $\bar{\delta}^\varepsilon(\bar{\rho})$ needs to be calibrated for all the densities $\bar{\rho} \in [0, 1]$. In practice, it suffices to calibrate the value of $\bar{\delta}^\varepsilon(\bar{\rho})$ for a discrete set of density values and then interpolate among those. In this work, we calibrate the values of $\bar{\delta}^\varepsilon(\bar{\rho})$ for $\bar{\rho} = \{0, 0.1, 0.2, 0.3, 0.4, 0.5, 0.6, 0.7, 0.8, 0.9, 1\}$ and use them to derive the interpolation relationship, say

$$\bar{\delta}^\varepsilon(\bar{\rho}) = \tilde{\delta}(\bar{\rho}; E, \nu, \sigma_{ts}, \sigma_{cs}, G_c, \varepsilon), \tag{17}$$

for the rest of values $\bar{\rho} \in [0, 1]$.

For the reader's convenience, we close this subsection by summarizing in Table 1 the proposed interpolation rules for all material constants.

3.3. The proposed multi-objective topology optimization formulation

At this stage, having introduced the design parameterization and interpolation rules for all of the material properties, we are in a position to spell out the multi-objective function whose maximization defines the optimal fracture response of structures.

Precisely, we seek to identify structures that

- exhibit a sufficiently large initial stiffness,
- delay the onset of fracture nucleation, and
- dissipate as much energy as possible once the fracture has occurred.

To do so, we introduce the multi-objective function

$$J = \omega_e \Pi_e - \omega_f \Pi_f + \omega_w \Pi_w \quad \text{with} \quad \begin{cases} \Pi_e(\bar{\rho}, \mathbf{u}, v) = \int_0^{t_n} \int_{\Omega} v^2 \bar{W}(\mathbf{E}(\mathbf{u}); \bar{\rho}) \, d\mathbf{X} \, dt \\ \Pi_f(\bar{\rho}, v) = \int_0^{t_n} \int_{\Omega} \frac{3\bar{G}_c(\bar{\rho})}{8} \left(\frac{1-v}{\varepsilon} + \varepsilon \nabla v \cdot \nabla v \right) \, d\mathbf{X} \, dt \\ \Pi_w(\bar{\rho}, \mathbf{u}, v) = \int_{t_n}^T \int_{\partial\Omega} \left[v^2 \frac{\partial \bar{W}}{\partial \mathbf{E}}(\mathbf{E}(\mathbf{u}); \bar{\rho}) \mathbf{N} \right] \cdot \mathbf{u} \, d\mathbf{X} \, dt \end{cases} \tag{18}$$

and consider the optimization problem

$$\begin{cases} \text{maximize} & J(\bar{\rho}, \mathbf{u}(\mathbf{X}, t; \bar{\rho}), v(\mathbf{X}, t; \bar{\rho})) \\ & 0 \leq \bar{\rho} \leq 1 \\ \text{subject to} & \begin{cases} g(\bar{\rho}) := |\Omega|^{-1} \int_{\Omega} \bar{\rho} \, d\mathbf{X} - V^* \leq 0 \\ (\mathbf{u}, v) \text{ solution of the phase-field equations (8)–(9).} \end{cases} \end{cases} \tag{19}$$

In these expressions, $\omega_e, \omega_f, \omega_w$ are weighting factors of choice such that $\omega_e + \omega_f + \omega_w = 1$ and $t_n \in [0, T]$ stands for a time of choice within the entire time period over which the structure is loaded. The first part Π_e in the multi-objective function (18) is nothing more than the total elastic energy stored by the structure from the beginning of the loading process until the chosen time t_n . Its maximization controls the initial stiffness of the structure. The second part Π_f in (18) is a measure² of the energy dissipated by the appearance of cracks from the beginning of the loading process until the chosen time t_n . Its minimization thus results in delaying the instance at which fracture first nucleates. The third part Π_w in the multi-objective function (18) denotes the work done by the applied forces from the chosen time t_n until the end of the loading process. Its maximization then serves to maximize the energy dissipated by fracture propagation once fracture nucleation has occurred. Finally, V^* in the inequality constraint (19)₂ denotes the maximum volume fraction of the actual material that is permitted to be present in the design. Fig. 2 provides a schematic of the physical meaning of the three sub-objectives Π_e, Π_f , and Π_w .

² As opposed to the classical phase-field theory wherein the quantity $S = \int_{\Omega} 3/8[(1-v)/\varepsilon + \varepsilon \nabla v \cdot \nabla v] \, d\mathbf{X}$ represents exactly the surface of cracks, in the context of the phase-field theory (8)–(9), S scales with the surface of cracks but is *not* exactly equal to it.

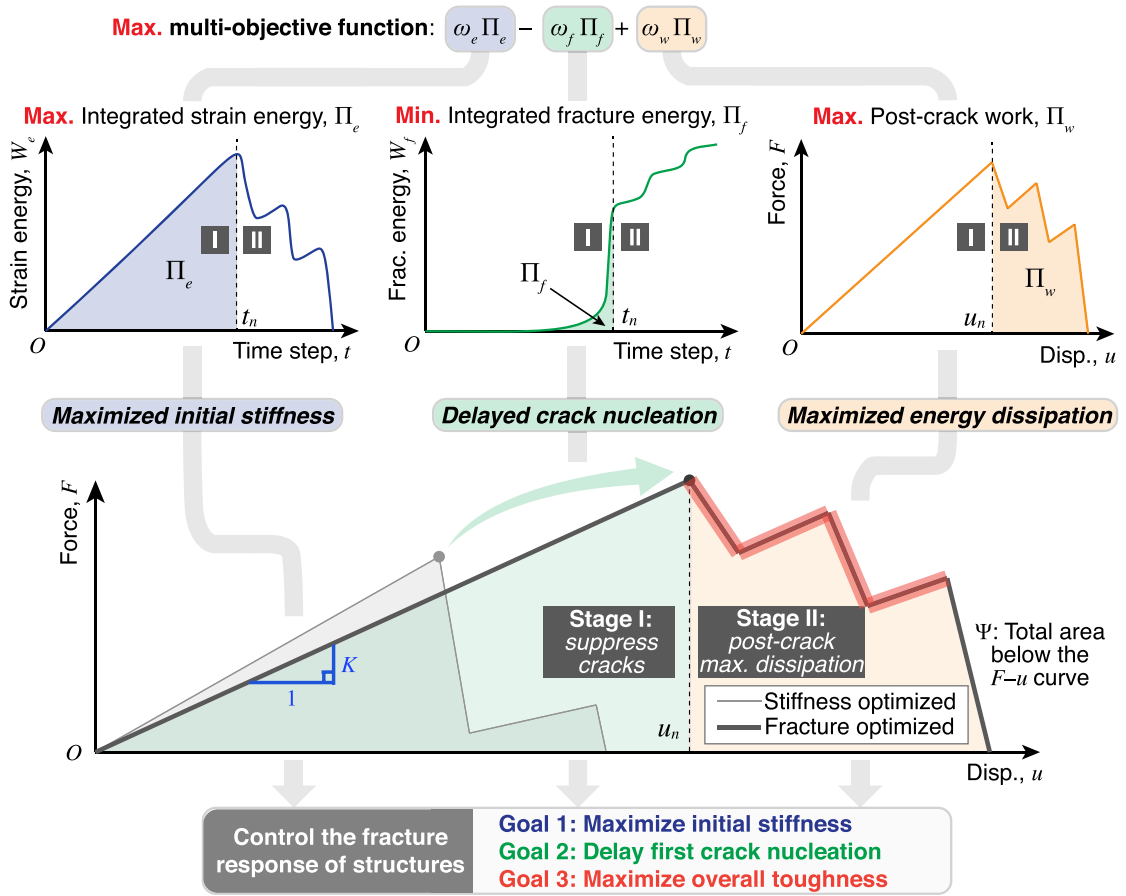


Fig. 2. Schematic of the proposed multi-objective function and its maximization leading to structures with optimized fracture response. The schematic includes a comparison between the force–displacement response of a structure optimized with the proposed framework and that of a structure optimized by conventional stiffness maximization.

The multi-objective function (18) generalizes several objective functions that have been recently utilized in the literature to optimize the fracture response of structures. Specifically, the multi-objective function (18) reduces to those put forth in Russ and Waisman (2020) and Desai et al. (2022) by setting $t_n = T$, while it reduces to those in Da and Yvonnet (2020) and Li et al. (2021) by setting $t_n = 0$. Note that the choice $t_n = T$ may promote the prevention of any crack and hence may lead to designs that are stiff but that catastrophically fail at the first nucleation of fracture. On the other hand, the choice $t_n = 0$ may promote the presence of too many cracks and hence may lead to designs that fail prematurely. The ability to choose the value of t_n as well as the weighting factors $\omega_e, \omega_f, \omega_w$ in the multi-objective function (18) allows greater flexibility to identify structures with the desired type of fracture performance.

3.4. Numerical implementation

In order to solve the optimization problem (19), we make use of the adjoint method (Bendsoe and Sigmund, 2003) to carry out the pertinent sensitivity analysis. The basic details are provided in Appendix B.1. In Appendix B.2, we also present numerical results aimed at verifying the accuracy of the sensitivity analysis. The computation of the time-dependent coupled PDEs (8)–(9) is carried out by means of a FE approach with a staggered solver; see Remark 3. Moreover, we make use of the well-established method of moving asymptotes (MMA) (Svanberg, 1987) to update the design variable ρ . Algorithm 1 provides an outline of the solution procedure. The implementation is carried out in the open-source computing platform FEniCSx (Scroggs et al., 2022). Specifically, for solving the coupled PDEs (8)–(9), we set the maximum staggered iteration as 100 and the relative tolerance for both the displacement and phase fields as 10^{-6} . In each staggered iteration, we further use the lower–upper (LU) decomposition to directly solve (8) and use a Newton–Raphson scheme to iteratively solve (9) with the generalized minimal residual (GMRES) method. All the computations are performed in parallel.

Algorithm 1: Overview of the solution procedure for the optimization problem (19)

```

1 Inputs: Optimization iteration counter,  $m = 1$ ; maximum iteration,  $m^{max}$ ; the initial value of design variable,  $\rho = \rho_0$ ;
2 while  $m \leq m^{max}$  do
3   Apply the density filter (Eq. (7)) on the design variable,  $\rho$ , to obtain the filtered variable,  $\bar{\rho}$ ;
4   Apply the Heaviside projection (Eq. (6)) on the filtered design variable,  $\bar{\rho}$ , to obtain the physical variable,  $\bar{\rho}$ ;
5   Obtain the material constants ( $\bar{E}$ ,  $\bar{\sigma}_{ts}$ ,  $\bar{\sigma}_{cs}$ ,  $\bar{G}_c$ ,  $\bar{\delta}^\epsilon$ ) through the proposed interpolation relationships (Eqs. (11), (13),
   (14), (17)) based on the physical design variable,  $\bar{\rho}$ ;
6   Solve numerically via FE the displacement field,  $\mathbf{u}(\mathbf{X}, t; \bar{\rho})$ , and the phase field,  $v(\mathbf{X}, t; \bar{\rho})$ , based on the material properties
   ( $\bar{E}$ ,  $\bar{\sigma}_{ts}$ ,  $\bar{\sigma}_{cs}$ ,  $\bar{G}_c$ ,  $\bar{\delta}^\epsilon$ );
7   Based on the field variables,  $\mathbf{u}(\mathbf{X}, t; \bar{\rho})$  and  $v(\mathbf{X}, t; \bar{\rho})$ , compute the function values,  $J$  and  $g$ , and perform the sensitivity
   analysis (the detailed procedure is given in Appendix B.1) to obtain the function gradients,  $dJ/d\rho$  and  $dg/d\rho$ , with
   respect to the design variable,  $\rho$ ;
8   Utilize the MMA optimizer to update the design variable,  $\rho$ , based on the function values,  $J$  and  $g$ , as well as the
   gradient information,  $dJ/d\rho$  and  $dg/d\rho$ ;
9    $m \leftarrow m + 1$ ;
10 end

```

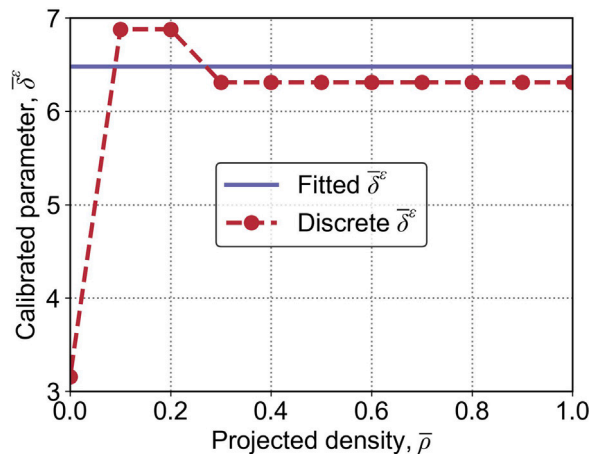


Fig. 3. The dimensionless parameter $\bar{\delta}^\epsilon(\bar{\rho})$ as a function of the density $\bar{\rho}$ for the material constants and regularization length listed in Table 2.

4. Sample results

In the sequel, we deploy the density-based framework introduced in the preceding section to examine the optimization of the fracture response of structures. With the objective of exploring a wide range of possible behaviors, we consider problems in which fracture nucleation is bound to occur in three different types of regions within the structure: within the bulk, from geometric singularities (pre-existing cracks and sharp corners), and from smooth parts of the boundary. More specifically, Examples 1 and 2 in Sections 4.1 and 4.2 deal with structures where fracture nucleation takes place from pre-existing cracks and sharp corners. Example 1 also serves to showcase the effects that the choice of time t_n has on the optimization process. On the other hand, Examples 3 and 4 in Sections 4.3 and 4.4 deal with structures where fracture nucleation takes place within the bulk or from smooth parts of the boundary. In addition, Example 4 serves to showcase the effects that the choice of weighting factors ω_c , ω_f , ω_w has on the final design. In all four examples, we use symmetric meshes to discretize domains and ensure symmetric topology ($\bar{\rho}$) by applying projection techniques. In Appendix C.2, we use Dsg. 11 to briefly illustrate the influence in structural behaviors by using symmetry and asymmetric meshes. We also restrict attention to structures made of homogeneous materials with deterministic material properties. For this reason, it is possible that symmetric patterns of cracks may appear in the simulations. The incorporation of stochastic material properties — in particular, stochastic strength properties — in the optimization process would likely rule out the existence of such symmetric solutions, however, this is beyond the scope of this work.

Table 2 summarizes the numerical values of the parameters entering the optimization problem used in all four examples. These values correspond to a modification of the parameters used in Kumar et al. (2020) for graphite; the modification is such that $E \leftarrow E/10$ and $G_c \leftarrow 10G_c$. Generally, a smaller Young’s modulus, E , results in smaller structural stiffness and could delay the process of maximum stress reaching the strength surface, which causes fracture nucleation. A larger critical energy release rate, G_c , requires more input energy to propagate the same length of the crack. Based on these two observations, we made these changes $E \leftarrow E/10$ and $G_c \leftarrow 10G_c$ in this work aiming at favoring a more balanced competition between fracture nucleation and propagation. Also,

Table 2
Summary of the parameters used for all four sample results in Sections. 4.1 through 4.4.

Inputs in the optimization problem	Values of the associated parameters
Young's modulus $\bar{E}(\bar{\rho})$	$E = 980$ MPa $\eta_E = 10^{-5}$ $p_E = 3$
Poisson's ratio $\bar{\nu}(\bar{\rho})$	$\nu = 0.13$
Tensile strength $\bar{\sigma}_{ts}(\bar{\rho})$	$\sigma_{ts} = 27$ MPa $\eta_{\sigma_{ts}} = 10^{-5}$ $p_{\sigma} = 2.5$
Compressive strength $\bar{\sigma}_{cs}(\bar{\rho})$	$\sigma_{cs} = 77$ MPa $\eta_{\sigma_{cs}} = 3.51 \times 10^{-6}$ $p_{\sigma} = 2.5$
Toughness $\bar{G}_c(\bar{\rho})$	$G_c = 0.91$ N/mm $\eta_{G_c} = 10^{-5}$ $p_{G_c} = 2$
Regularization length ϵ	$\epsilon = 0.15$ mm
Calibrated parameter $\bar{\delta}^\epsilon(\bar{\rho})$	$\bar{\delta}^\epsilon = 6.48$

note that the regularization length is set at $\epsilon = 0.15$ mm for all four examples, which was checked to be small enough as required. For this value of ϵ and all $\bar{\rho} \in [0, 1]$, note as well that the dimensionless parameter is set at the constant value $\bar{\delta}^\epsilon = 6.48$. This last prescription merits clarification. Fig. 3 shows the values of $\bar{\delta}^\epsilon(\bar{\rho})$ for $\bar{\rho} = \{0, 0.1, 0.2, 0.3, 0.4, 0.5, 0.6, 0.7, 0.8, 0.9, 1\}$ as obtained from the calibration procedure laid out in Section 4.3.2 of Kumar et al. (2020). While $\bar{\delta}^\epsilon(\bar{\rho})$ is *not* a constant, it is nearly so for $\bar{\rho} \geq 0.1$. However, the influence of the value of $\bar{\delta}^\epsilon(\bar{\rho})$ in the optimization process is negligible when $\bar{\rho} \leq 0.1$; this is because the material then is essentially “air”. For this reason, we choose to idealize $\bar{\delta}^\epsilon(\bar{\rho})$ as the constant value $\bar{\delta}^\epsilon = 6.48$. Unless otherwise stated, the maximum optimization iteration is $m^{max} = 600$ in all the calculations that follow. The sharpness parameter in the Heaviside projection (6) is initially set at $\beta = 1$. Starting from the optimization iteration $m = 181$, the β value is doubled every 60 iterations until $\beta = 128$. The threshold value is set at $\theta = 0.5$, as mentioned previously. Finally, all the calculations are carried out under plane-stress conditions.

4.1. A pre-cracked beam under three-point bending

In this subsection, we consider the optimization of a pre-cracked beam under three-point bending, namely, a pre-cracked Messerschmitt-Bölkow-Blohm (MMB) beam. Fig. 4(a) shows a schematic of the design domain, which contains a 1.2-mm-long pre-existing crack on the bottom, and the applied boundary displacements. The design variable is fixed at $\rho \equiv 1$ on the three indicated non-designable regions around the two supports on the bottom and the applied displacement $u \propto t$ on the top. Also, the phase field is fixed at $v \equiv 1$ around two supports. Such a design domain is discretized by a mesh (axially symmetric with respect to 1/2 of the domain) with 107,200 bilinear quadrilateral finite elements of size $h = \epsilon/3 = 0.05$ mm. The maximum value of the applied displacement is $u_{max} = 2.72$ mm for the optimization process. We also carry out a post-optimization FE analysis to evaluate the resulting force–displacement curves to complete failure of the optimized structures. The maximum value of the applied displacement for those is $u_{max} = 3.60$ mm. For the topology-optimization-specific parameters, we use the filter radius $R = 1.2$ mm and allowable volume fraction $V^* = 0.45$. The weighting factors are set at $\omega_e = 0.20$, $\omega_f = 0.78$, and $\omega_w = 0.02$.

Fig. 4(b) presents the obtained designs — labeled Dsgs. 2 through 4 — for three different values of the time t_n , which correspond to applied displacements $u_n = 1.92, 2.16$, and 2.72 mm, respectively. The classical stiffness design — labeled Dsg. 1 — obtained from conventional stiffness maximization is also included in the figure for reference. Fig. 4(b) shows the physical density field $\bar{\rho}$ representing the optimized topology. Also, it shows contours of the phase field v (only plotted when $v \leq 0.5$) at $u_{max} = 3.60$ mm. The figure also includes the critical values of the applied displacement $u = u_c$ at which fracture first nucleates in each design. By comparing Dsg. 1 with Dsgs. 2–4, it can be observed that the pre-crack still exists in Dsg. 1, while it is replaced by rounded corners in Dsgs. 2–4. It is also interesting to note that the number of batches of crack nucleation in all designs is either one or two. By increasing u_n , the top and bottom major members are merged into one as shown in Dsg. 3, and finally, the merged major member is lifted as shown in Dsg. 4. This is because the tensile stress gets redistributed in these merging and lifting processes and fracture nucleation is, in turn, delayed.

Fig. 4(c) shows the force–displacement curves and the structural performance via a radar chart for Dsgs. 1–4. Several observations are worth pointing out. First, compared to Dsg. 1, the first nucleation of fracture occurs both at larger forces and larger displacements in Dsgs. 2 through 4. What is more, the overall toughness Ψ — defined as the area under the force–displacement curve — is also significantly larger (up to 230%) for all Dsgs. 2 through 4. In spite of delaying fracture and dissipating more energy by fracture propagation, Dsgs. 2–4 still exhibit a sufficiently large initial stiffness compared to that of Dsg. 1. In terms of the applied displacement, the increase of u_n leads to an increase in the delay of fracture nucleation.

Remark 5. The results shown in Fig. 4 were obtained by making use of a voxel-based mesh (fixed-grid method) (da Silva et al., 2019). In Appendix C.1, using Dsg. 2 as an example, we show that making use of a body-fitted mesh produces results in good agreement with the ones from the voxel-based mesh.

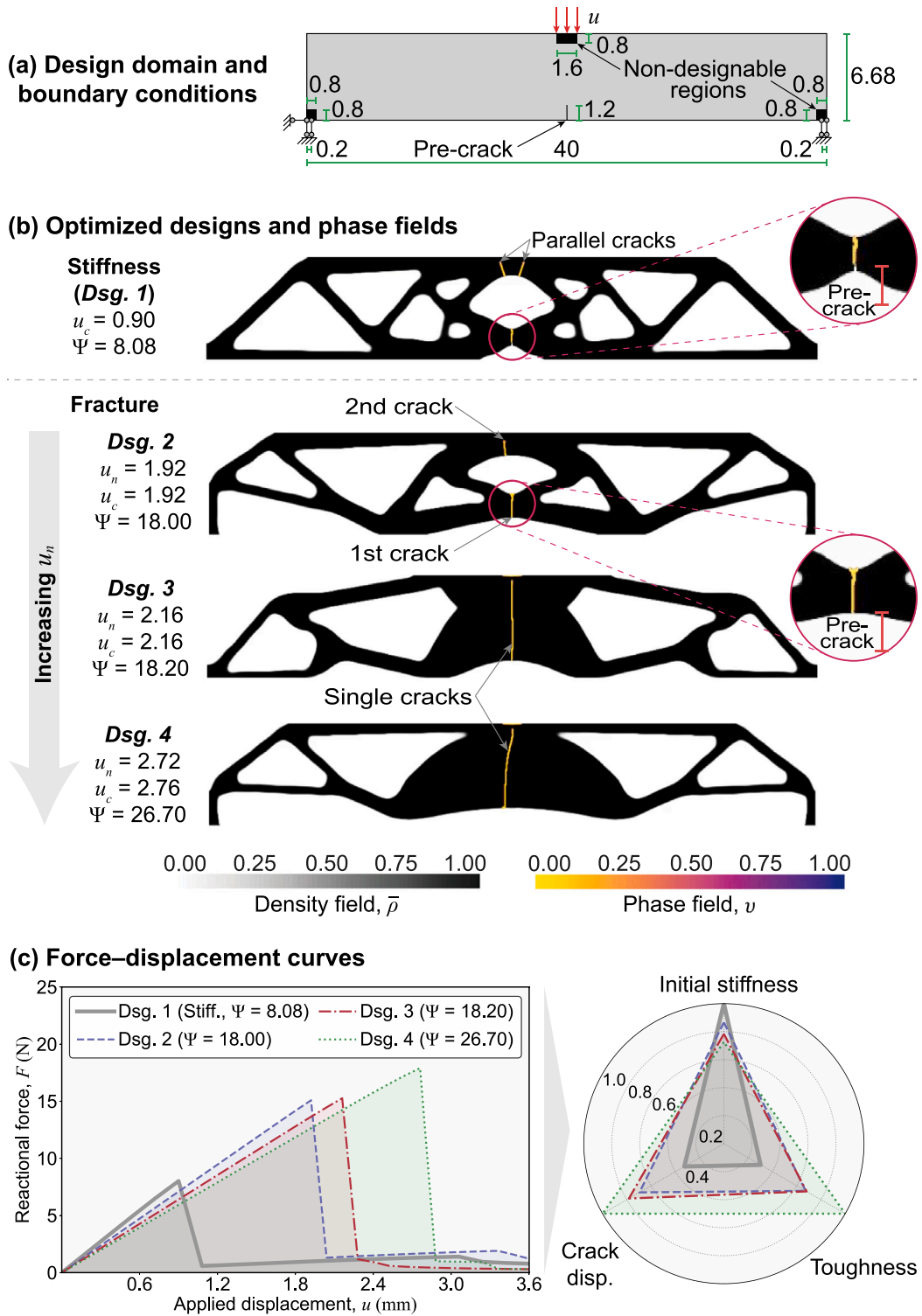


Fig. 4. Design setup and results for the optimization of a pre-cracked beam under three-point bending. (a) Design domain and boundary conditions (all length units are in mm). (b) Optimized designs (Dsgs. 2–4) and phase-field contours at $u_{max} = 3.60$ mm for three different values of displacement $u_n \propto t_n$. (c) Force–displacement curves for the optimized designs and corresponding radar chart comparing their normalized structural performance. The classical stiffness design (Dsg. 1) obtained from conventional stiffness maximization is included for reference.

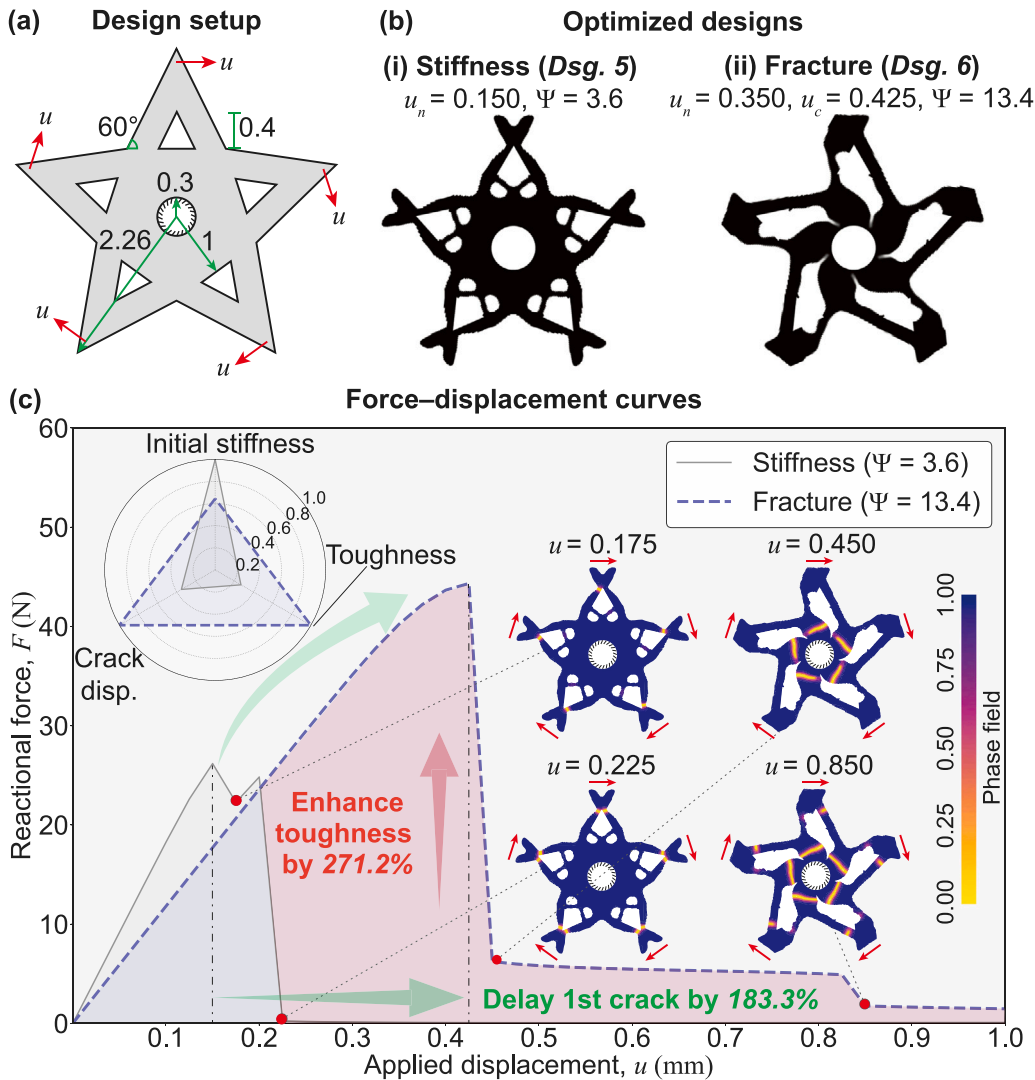


Fig. 5. Design setup and results for the optimization of a star-shaped plate under rotational displacement. (a) Design domain and boundary conditions (all length units are in mm). (b) Optimized designs. (c) Force–displacement curve for the optimized design. The classical stiffness design (Dsg. 5) obtained from conventional stiffness maximization is included for reference.

4.2. A star-shaped plate under rotational displacement

Next, we consider the optimization of a star-shaped plate, initially containing holes with sharp corners (in contrast to a pre-existing crack like the beam in the preceding subsection), subjected to a rotational displacement. The pertinent design domain and boundary conditions are depicted in Fig. 5(a). The phase field is fixed at $v \equiv 1$ in a 0.15 mm-thick ring around the circular support and at the five corners where the displacement $u \propto t$ is applied. The design domain is discretized with an unstructured mesh (rotationally symmetric with respect to $1/5$ of the domain) of 33,840 bilinear quadrilateral finite elements of size $h = \epsilon/10 = 0.015$ mm. The maximum values of the applied displacement are $u_{max} = 0.5$ mm for the optimization process and $u_{max} = 1.0$ mm for the post-optimization FE analysis that is carried out to evaluate the resulting force–displacement curves to complete failure of the optimized structures. For the topology-optimization-specific parameters, we use the filter radius $R = 0.15$ mm and allowable volume fraction $V^* = 0.5$. The weighting factors are set at $\omega_e = 0.15$, $\omega_f = 0.80$, and $\omega_w = 0.05$. Finally, we choose the time t_n such that $u_n = 0.35$ mm.

Fig. 5(b) presents the conventional design — labeled Dsg. 5 — obtained from stiffness maximization and the one — labeled Dsg. 6 — obtained from the proposed optimization. Interestingly, contrary to Dsg. 5, Dsg. 6 does not exhibit centrosymmetry around the regions of applied displacement. This is because the tensile and compressive strengths of the material are different. Another distinct feature is that corners in the fracture design Dsg. 6 — but not in the stiffness design Dsg. 5 — have been completely removed by the optimization process. Consequently, as shown by the force–displacement curves and the inset phase-field contours in Fig. 5(c), the stiffness design Dsg. 5 fails by nucleating fracture from the corners and it does so at a much smaller critical value u_c of the applied

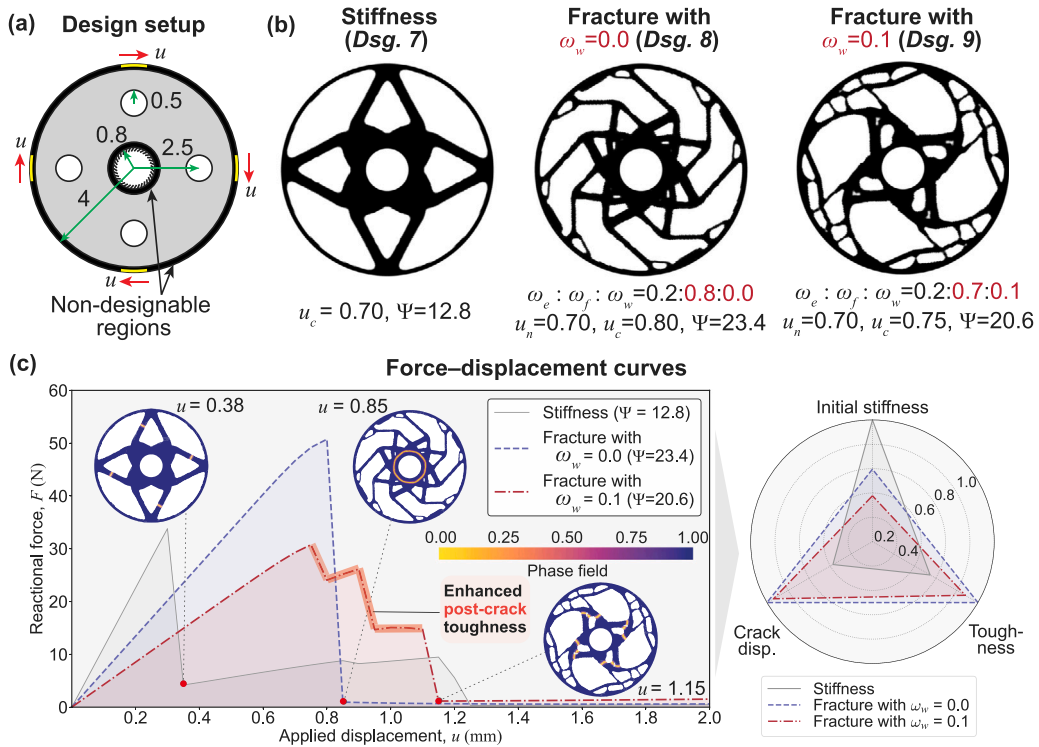


Fig. 6. Design setup and results for the optimization of a disk under rotational displacement. (a) Design domain and boundary conditions (all length units are in mm). (b) Optimized designs for two different choices of weighting factors $\omega_e, \omega_f, \omega_w$. (c) Force-displacement curves for the optimized designs and corresponding radar chart comparing their normalized structural performance. The classical stiffness design (Dsg. 7) obtained from conventional stiffness maximization is included for reference.

displacement (about 183.3% smaller) than that in Dsg. 6, wherein fracture nucleates from smooth boundaries near the circular support. What is more, Dsg. 6 dissipates significantly more energy (about 271.2% more) than Dsg. 5 by the propagation of fracture that leads to the complete failure of the structure.

4.3. A disk under rotational displacement

In this subsection, as shown in Fig. 6(a), we consider the optimization of a disk, initially containing circular holes, under a rotational displacement $u \propto t$ that is applied at four symmetric parts on the outer boundary. The design variable and phase field are fixed at $\rho \equiv 1$ and $\nu \equiv 1$ over two 2-mm-thick ring-shaped non-designable regions around the central and outer boundaries. The design domain is discretized with an unstructured mesh (rotationally symmetric with respect to 1/4 of the domain) of 42,472 bilinear quadrilateral finite elements of size $h = \varepsilon/5 = 0.03$ mm. The maximum values of the applied displacement are $u_{max} = 1.0$ mm for the optimization process and $u_{max} = 2.0$ mm for the post-optimization FE analysis of the optimized structures. Furthermore, the results are generated by using the filter radius $R = 0.2$ mm and the allowable volume fraction $V^* = 0.45$. The sharpness parameter β is doubled starting from the optimization iteration $m = 61$ (instead of $m = 181$) until $\beta = 64$ (instead of $\beta = 128$), and the time t_n is chosen such that $u_n = 0.7$ mm.

Fig. 6(b) presents the design — labeled Dsg. 7 — obtained from conventional stiffness maximization and two designs obtained from the proposed optimization framework. Specifically, Dsg. 8 corresponds to the choice of weighting factors $\omega_e = 0.2, \omega_f = 0.8, \omega_w = 0$, while Dsg. 9 corresponds to $\omega_e = 0.2, \omega_f = 0.7, \omega_w = 0.1$. Similar to the finding in the preceding subsection, the stiffness design Dsg. 7 features centrosymmetry while the fracture designs Dsgs. 8 and 9 do not. Again, this is because the tensile and compressive strengths of the material, which are different in value, are accounted for in the fracture designs. It is also interesting to note that Dsg. 9 — for which ω_w is not zero and hence for which the dissipation due to fracture propagation is partially maximized — is similar to the highly porous structures found in Zhao and Zhang (2021a,b). This is because the presence of many pores promotes the nucleation and renucleation of many cracks from the pore walls, which provide a toughening mechanism. To demonstrate the convergence of the optimized designs, we present the histories of the objective (J) and constraint (g) functions for Dsg. 8 as a representative example in Appendix B.3.

Fig. 6(c) compares the force-displacement curves of all three designs Dsgs. 7–9. The insets show the contours of the phase field at several times along the loading process. One immediate observation is that the overall toughness Ψ — defined, again, as the area under the force-displacement curve — is significantly larger for the fracture Dsgs. 8 and 9 than for the stiffness design (Dsg.

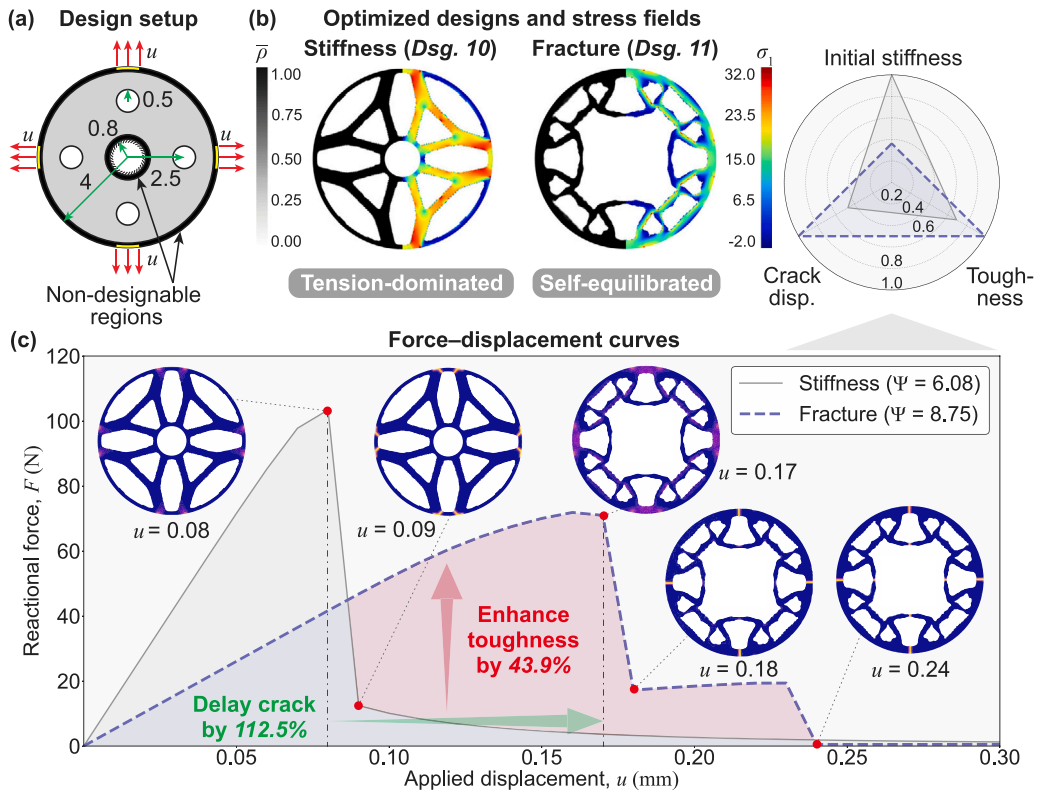


Fig. 7. Design setup and results for the optimization of a disk under biaxial tension. (a) Design domain and boundary conditions (all length units are in mm). (b) Optimized design and contours of the largest (in the magnitude sense) principal stress σ_1 (in MPa). (c) Force–displacement curves for the optimized design and corresponding radar chart of its normalized structural performance. The classical stiffness design (Dsg. 10) obtained from conventional stiffness maximization is included for reference.

7). The overall toughness in Dsg. 8 is the result of a delay in the first nucleation of fracture, which occurs at a significantly larger deformation and force than in the stiffness design Dsg. 7. The overall toughness in Dsg. 9 is due to multiple fracture nucleation events. Also, the first nucleation of fracture in Dsg. 9 occurs at a larger deformation although at a smaller force than in Dsg. 7.

4.4. A disk under biaxial tension

Finally, we consider the optimization of the same disk considered above but now subjected to biaxial tension instead of a rotational displacement. The design variable is fixed at $\rho \equiv 1$ over two 2-mm-thick ring-shaped non-designable regions around the central and outer boundaries. The phase field is fixed at $v \equiv 1$ only around the inner boundary. Fig. 7(a) provides a schematic of the design domain and the applied displacements $u \propto t$ on the outer boundary. The design domain is discretized with an unstructured mesh (axially symmetric with respect to 1/4 of the domain) of 42,472 bilinear quadrilateral finite elements of size $h = \epsilon/5 = 0.03$ mm. The maximum values of the applied displacement are $u_{max} = 0.20$ mm for the optimization process and $u_{max} = 0.30$ mm for the post-optimization FE analysis of the optimized structures. For the topology-optimization-specific parameters, we use the filter radius $R = 0.2$ mm, allowable volume fraction $V^* = 0.45$, weighting factors $\omega_e = 0.15$, $\omega_f = 0.80$, and $\omega_w = 0.05$, and time t_n such that $u_n = 0.15$ mm. The sharpness parameter β is doubled until $\beta = 32$ (instead of $\beta = 128$).

Fig. 7(b) presents the obtained design considering fracture and, for reference, the classical design obtained from conventional stiffness maximization; they are labeled Dsg. 11 and Dsg. 10, respectively. The left parts show the density field $\bar{\rho}$, while the right parts show contours of the largest (in the magnitude sense) principal stress σ_1 at the applied displacement $u = 0.08$ mm. Rather interestingly, the fracture design Dsg. 11 is a self-equilibrated ring-shaped structure that is fully detached from the middle support. While the stiffness design Dsg. 10 is dominated by tensile stresses, the fracture design Dsg. 11 favors the presence of compressive stresses.

Fig. 7(c) shows the force–displacement curves and the structural performance via a radar chart for Dsgs. 10 and 11. The insets show the contours of the phase field several times along the loading process. It is clear that the initial stiffness of Dsg. 10 is considerably larger than that of Dsg. 11. On the other hand, the first nucleation of fracture takes place at a significantly larger applied displacement with multiple fracture nucleation events in Dsg. 11, which also exhibits a larger overall toughness.

5. Final comments

The sample results presented in Section 4 provide ample encouraging evidence to continue studying the optimization framework proposed in this work — which, again, is built on a complete theory of fracture nucleation and propagation — in order to explore the optimization of the fracture response of structures subjected to quasistatic mechanical loads.

The results have also served to make clear that the traditional design of structures based on stiffness maximization leads to structures with poor fracture responses. In addition, the optimized structures considering fracture have revealed a variety of strengthening and toughening mechanisms. For example, depending on the elastic, strength, and toughness properties of the material and the applied loads, it may be more advantageous to replace pre-existing cracks with rounded corners. The same may be true for sharp corners. The use of structures without centrosymmetry may be preferred when the tensile and compressive strengths of the material are very different. The presence of numerous pores may also render structures with tougher overall behaviors as they may lead to multiple nucleation and renucleation events from the pore walls.

An obvious next step is to confront the optimized designs generated by the proposed framework with experiments in order to validate their performance. We are currently working in this direction. Another direction of interest would be to transcribe the strengthening and toughening mechanisms found here to the realm of microstructures in order to design new materials with enhanced fracture properties.

CRedit authorship contribution statement

Yingqi Jia: Methodology, Investigation, Software, Writing – original draft, Writing – review & editing. **Oscar Lopez-Pamies:** Conceptualization, Methodology, Investigation, Writing – original draft, Writing – review & editing, Funding acquisition. **Xiaoqia Shelly Zhang:** Conceptualization, Methodology, Investigation, Writing – original draft, Writing – review & editing, Funding acquisition, Resources, Supervision.

Declaration of competing interest

The authors declare that they have no known competing financial interests or personal relationships that could have appeared to influence the work reported in this paper.

Data availability

Data will be made available on request.

Acknowledgments

This work was supported by the National Science Foundation, United States through the EAGER Grant CMMI-2127134. This support is gratefully acknowledged.

Appendix A. The scaling function $s(\bar{\rho})$

As pointed out in Section 3.2.3, the fact that the phase-field equations (8)–(9) contain as material inputs the Young's modulus $\bar{E}(\bar{\rho})$, the tensile and compressive strengths $\bar{\sigma}_{ts}(\bar{\rho})$ and $\bar{\sigma}_{cs}(\bar{\rho})$, and the critical energy release rate $\bar{G}_c(\bar{\rho})$ implies that they feature a built-in range of material length scales (morally speaking, the length scales of the process zones). Taking the tensile strength $\bar{\sigma}_{ts}(\bar{\rho})$ as the dominant strength parameter, that range of material lengths can be reduced to the single characteristic material length scale

$$\varepsilon_c(\bar{\rho}) = \frac{3\bar{E}(\bar{\rho})\bar{G}_c(\bar{\rho})}{8\bar{\sigma}_{ts}^2(\bar{\rho})}.$$

In this context, it is reasonable to enforce that this characteristic length scale remains the same in the design domain irrespective of the value of the density $\bar{\rho}$.

To this end, we begin by introducing the intermediate characteristic length

$$\hat{\varepsilon}_c(\bar{\rho}) = \frac{3\hat{E}(\bar{\rho})\hat{G}_c(\bar{\rho})}{8\hat{\sigma}_{ts}^2(\bar{\rho})}$$

in terms of the classical modified SIMP rules (Bendsøe and Sigmund, 1999)

$$\begin{cases} \hat{E}(\bar{\rho}) = (\eta_E + (1 - \eta_E)\bar{\rho}^{p_E}) E \\ \hat{G}_c(\bar{\rho}) = (\eta_{G_c} + (1 - \eta_{G_c})\bar{\rho}^{p_{G_c}}) G_c \\ \hat{\sigma}_{ts}(\bar{\rho}) = (\eta_{\sigma_{ts}} + (1 - \eta_{\sigma_{ts}})\bar{\rho}^{p_{\sigma}}) \sigma_{ts} \end{cases}.$$

By defining the scaling function

$$s(\bar{\rho}) := \frac{\hat{\varepsilon}_c(\bar{\rho})}{\hat{\varepsilon}_c(1)} = \frac{3\hat{E}(\bar{\rho})\hat{G}_c(\bar{\rho})}{8\bar{\sigma}_{ts}^2(\bar{\rho})} \frac{8\bar{\sigma}_{ts}^2(1)}{3\hat{E}(1)\hat{G}_c(1)} = \frac{(\eta_E + (1 - \eta_E)\bar{\rho}^{p_E}) (\eta_{G_c} + (1 - \eta_{G_c})\bar{\rho}^{p_{G_c}})}{(\eta_{\sigma_{ts}} + (1 - \eta_{\sigma_{ts}})\bar{\rho}^{p_\sigma})^2}$$

and using the proposed interpolation rules (11), (13), (14) in the main body of the text, it follows that

$$\varepsilon_c(\bar{\rho}) = \frac{3 \frac{1}{\sqrt{s(\bar{\rho})}} (\eta_E + (1 - \eta_E)\bar{\rho}^{p_E}) E \frac{1}{\sqrt{s(\bar{\rho})}} (\eta_{G_c} + (1 - \eta_{G_c})\bar{\rho}^{p_{G_c}}) G_c}{8 \left[(\eta_{\sigma_{ts}} + (1 - \eta_{\sigma_{ts}})\bar{\rho}^{p_\sigma}) \sigma_{ts} \right]^2} = \frac{3EG_c}{8\sigma_{ts}^2} = \text{constant}$$

as desired.

Now, taking into account that the modified SIMP rules (\hat{E} and \hat{G}_c) effectively penalize the intermediate physical density, $\bar{\rho} \in (0, 1)$, and guarantee that the interpolated material properties satisfy the physical bounds, it is also reasonable to require that the proposed interpolation rules (\bar{E} and \bar{G}_c) deviate as little as possible from \hat{E} and \hat{G}_c . That is, we want that $s(0) = s(1) = 1$ and that, for $\bar{\rho} \in (0, 1)$, $s(\bar{\rho}) \approx 1$. This is accomplished by the prescriptions (15)–(16) introduced in the main body of the text.

Appendix B. Sensitivity analysis and convergence histories

B.1. The general procedure of sensitivity analysis

In this appendix, we outline the sensitivity analysis used to solve the optimization problem (19). First, in order to deal with the inequalities in (9), following Section 4.1 in Kumar et al. (2018a), we use a penalty method and rewrite

$$\text{Div} \left[\varepsilon \bar{G}_c(\bar{\rho}) \nabla v \right] = \frac{8}{3} v \bar{W}(\mathbf{E}(\mathbf{u}); \bar{\rho}) - \frac{4}{3} c_e(\mathbf{X}, t; \bar{\rho}) - \frac{\bar{G}_c(\bar{\rho})}{2\varepsilon} + \frac{4}{3} \frac{\partial \bar{W}_v(v; \bar{\rho})}{\partial v}, \quad (\mathbf{X}, t) \in \Omega \times [0, T], \tag{B.1}$$

where

$$\bar{W}_v(v; \bar{\rho}) = \frac{\bar{\alpha}(\bar{\rho})}{2} \left[(|v| - v)^2 + (|1 - v| - (1 - v))^2 \right]$$

with

$$\bar{\alpha}(\bar{\rho}) = 10^3 \max \left\{ \frac{\bar{G}_c(\bar{\rho})}{\varepsilon}, \frac{3\bar{G}_c(\bar{\rho})\bar{\delta}^\varepsilon(\bar{\rho})}{8\varepsilon} \right\}.$$

Given the coupled PDEs in (8) and (B.1), we can perform the standard FE analysis and derive the corresponding matrix forms. We define $\mathbf{U}_k(\bar{\rho})$ and $\mathbf{V}_k(\bar{\rho})$ as global displacement and phase field vectors associated with the physical density vector $\bar{\rho}$ at the time step t_k , respectively. We also denote $\mathbf{R}_{\mathbf{U},k} = \mathbf{R}_{\mathbf{U}}(\bar{\rho}, \mathbf{U}_k(\bar{\rho}), \mathbf{V}_k(\bar{\rho}))$ and $\mathbf{R}_{\mathbf{V},k} = \mathbf{R}_{\mathbf{V}}(\bar{\rho}, \mathbf{U}_k(\bar{\rho}), \mathbf{V}_k(\bar{\rho}))$ as global residual vectors for (8) and (B.1) at the time step t_k , respectively. Then we can evaluate the sensitivity of the objective and constraint functions with respect to the design variables by using the adjoint method (Bendsoe and Sigmund, 2003). Specifically, the Lagrangian

$$\hat{f}(\bar{\rho}, \mathbf{U}_0(\bar{\rho}), \mathbf{U}_1(\bar{\rho}), \dots, \mathbf{U}_M(\bar{\rho}), \mathbf{V}_0(\bar{\rho}), \mathbf{V}_1(\bar{\rho}), \dots, \mathbf{V}_M(\bar{\rho}))$$

of any time-discretized objective or constraint function

$$f(\bar{\rho}, \mathbf{U}_0(\bar{\rho}), \mathbf{U}_1(\bar{\rho}), \dots, \mathbf{U}_M(\bar{\rho}), \mathbf{V}_0(\bar{\rho}), \mathbf{V}_1(\bar{\rho}), \dots, \mathbf{V}_M(\bar{\rho}))$$

can be constructed as

$$\begin{aligned} & \hat{f}(\bar{\rho}, \mathbf{U}_0(\bar{\rho}), \mathbf{U}_1(\bar{\rho}), \dots, \mathbf{U}_M(\bar{\rho}), \mathbf{V}_0(\bar{\rho}), \mathbf{V}_1(\bar{\rho}), \dots, \mathbf{V}_M(\bar{\rho})) \\ &= f(\bar{\rho}, \mathbf{U}_0(\bar{\rho}), \mathbf{U}_1(\bar{\rho}), \dots, \mathbf{U}_M(\bar{\rho}), \mathbf{V}_0(\bar{\rho}), \mathbf{V}_1(\bar{\rho}), \dots, \mathbf{V}_M(\bar{\rho})) + \sum_{k=0}^M (\lambda_{\mathbf{U},k} \mathbf{R}_{\mathbf{U},k}) + \sum_{k=0}^M (\lambda_{\mathbf{V},k} \mathbf{R}_{\mathbf{V},k}) \end{aligned} \tag{B.2}$$

where the parameters $\lambda_{\mathbf{U},k}$ and $\lambda_{\mathbf{V},k}$ for $k = 0, 1, \dots, M$ are arbitrary adjoint vectors to be determined.

Taking the derivative of (B.2) with respect to the density $\bar{\rho}_e$ of the element e yields

$$\begin{aligned} \frac{d\hat{f}}{d\bar{\rho}_e} &= \frac{\partial f}{\partial \bar{\rho}_e} + \sum_{k=0}^M \left(\frac{\partial f}{\partial \mathbf{U}_k} \frac{\partial \mathbf{U}_k}{\partial \bar{\rho}_e} + \frac{\partial f}{\partial \mathbf{V}_k} \frac{\partial \mathbf{V}_k}{\partial \bar{\rho}_e} \right) \\ &+ \sum_{k=0}^M \left[\lambda_{\mathbf{U},k} \left(\frac{\partial \mathbf{R}_{\mathbf{U},k}}{\partial \bar{\rho}_e} + \frac{\partial \mathbf{R}_{\mathbf{U},k}}{\partial \mathbf{U}_k} \frac{\partial \mathbf{U}_k}{\partial \bar{\rho}_e} + \frac{\partial \mathbf{R}_{\mathbf{U},k}}{\partial \mathbf{V}_k} \frac{\partial \mathbf{V}_k}{\partial \bar{\rho}_e} \right) \right] \\ &+ \sum_{k=0}^M \left[\lambda_{\mathbf{V},k} \left(\frac{\partial \mathbf{R}_{\mathbf{V},k}}{\partial \bar{\rho}_e} + \frac{\partial \mathbf{R}_{\mathbf{V},k}}{\partial \mathbf{U}_k} \frac{\partial \mathbf{U}_k}{\partial \bar{\rho}_e} + \frac{\partial \mathbf{R}_{\mathbf{V},k}}{\partial \mathbf{V}_k} \frac{\partial \mathbf{V}_k}{\partial \bar{\rho}_e} \right) \right]. \end{aligned}$$

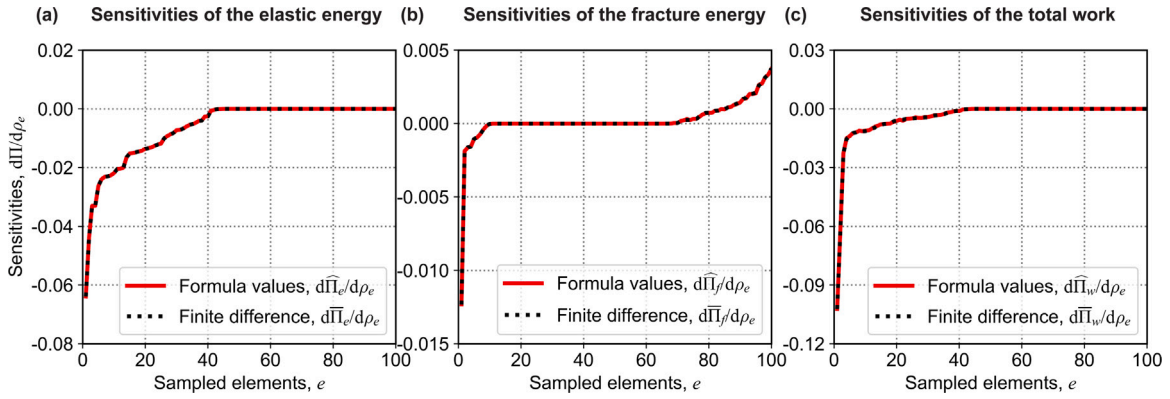


Fig. B.8. Comparisons of the sensitivities of the (a) elastic energy (Π_e), (b) fracture energy (Π_f), and (c) total work (Π_w) obtained from the proposed formula and the finite difference analysis. For each pair of comparisons, 100 finite elements are randomly sampled and the final sensitivities are sorted in increasing order for better visualization.

Rearranging terms renders

$$\begin{aligned} \frac{d\hat{f}}{d\rho_e} &= \frac{\partial f}{\partial \rho_e} + \sum_{k=0}^M \left(\lambda_{U,k} \frac{\partial \mathbf{R}_{U,k}}{\partial \rho_e} + \lambda_{V,k} \frac{\partial \mathbf{R}_{V,k}}{\partial \rho_e} \right) \\ &+ \sum_{k=0}^M \left\{ \left[\frac{\partial f}{\partial \mathbf{U}_k} + \left(\frac{\partial \mathbf{R}_{U,k}}{\partial \mathbf{U}_k} \right)^\top \lambda_{U,k} + \left(\frac{\partial \mathbf{R}_{V,k}}{\partial \mathbf{U}_k} \right)^\top \lambda_{V,k} \right] \frac{\partial \mathbf{U}_k}{\partial \rho_e} \right\} \\ &+ \sum_{k=0}^M \left\{ \left[\frac{\partial f}{\partial \mathbf{V}_k} + \left(\frac{\partial \mathbf{R}_{U,k}}{\partial \mathbf{V}_k} \right)^\top \lambda_{U,k} + \left(\frac{\partial \mathbf{R}_{V,k}}{\partial \mathbf{V}_k} \right)^\top \lambda_{V,k} \right] \frac{\partial \mathbf{V}_k}{\partial \rho_e} \right\}. \end{aligned}$$

At this stage, we can solve for the adjoint vectors $\lambda_{U,k}$ and $\lambda_{V,k}$ by eliminating the coefficients of the computationally expensive terms $\partial \mathbf{U}_k / \partial \rho_e$ and $\partial \mathbf{V}_k / \partial \rho_e$. We then have

$$\frac{d\hat{f}}{d\rho_e} = \frac{\partial f}{\partial \rho_e} + \sum_{k=0}^M \left(\lambda_{U,k} \frac{\partial \mathbf{R}_{U,k}}{\partial \rho_e} + \lambda_{V,k} \frac{\partial \mathbf{R}_{V,k}}{\partial \rho_e} \right).$$

Finally, the sensitivities with respect to the physical density vector can be expressed in tensorial form as

$$\frac{d\hat{f}}{d\bar{\rho}} = \frac{\partial f}{\partial \bar{\rho}} + \sum_{k=0}^M \left[\left(\frac{\partial \mathbf{R}_{U,k}}{\partial \bar{\rho}} \right)^\top \lambda_{U,k} + \left(\frac{\partial \mathbf{R}_{V,k}}{\partial \bar{\rho}} \right)^\top \lambda_{V,k} \right].$$

To compute the sensitivities with respect to the design density vector $d\hat{f}/d\rho$, one simply needs to apply the chain rule. It should be noted that the history dependence is explicitly considered through the time-dependent displacement fields, $\mathbf{U}_0, \mathbf{U}_1, \dots, \mathbf{U}_M$, and phase fields, $\mathbf{V}_0, \mathbf{V}_1, \dots, \mathbf{V}_M$.

B.2. Sensitivity verification

To verify the accuracy of the sensitivity analysis of this work, we compare the sensitivities obtained from the derived formula ($d\hat{f}/d\rho$) and the finite difference method ($d\bar{f}/d\rho$). The sensitivity of the element e obtained from the finite difference method can be expressed as

$$\frac{d\bar{f}}{d\rho_e} = \frac{f(\rho + \eta) - f(\rho)}{\eta},$$

where η is a moderately small perturbation ($\eta = 10^{-5}$ is used herein) to balance the truncation and rounding errors. All the entries of the vector η are equal to 0 except that the e th entry is η . Specifically, we use the Dsg. 8 as a representative example to perform the sensitivity verification. We randomly sample 100 finite elements satisfying the uniform distribution, and then separately compute the sensitivities of the elastic energy (Π_e), fracture energy (Π_f), and total work (Π_w) in the multi-objective function (Eq. (18)) with respect to the design variable, ρ . The comparisons of sensitivities obtained from the derived formula ($d\hat{\Pi}_e/d\rho$, $d\hat{\Pi}_f/d\rho$, and $d\hat{\Pi}_w/d\rho$) and the finite difference method ($d\bar{\Pi}_e/d\rho$, $d\bar{\Pi}_f/d\rho$, and $d\bar{\Pi}_w/d\rho$) are shown in Fig. B.8. It can be observed that the difference between the sensitivities obtained from the derived formula and the finite difference analysis is negligible. Also, the relative 2-norms of errors of the sensitivities of Π_e , Π_f , and Π_w are 7.39×10^{-6} , 1.01×10^{-4} , and 9.10×10^{-5} , respectively, indicating the accuracy of the sensitivity analysis in Appendix B.1.

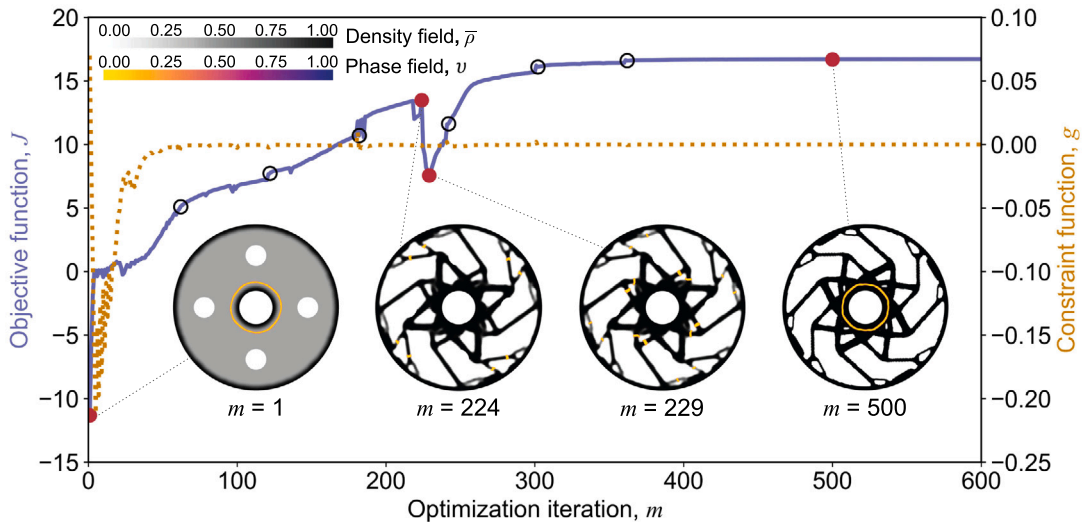


Fig. B.9. Convergence histories of the objective (J) and constraint (g) functions. Four representative intermediate density fields ($\bar{\rho}$) and the associated phase fields (v , plotted only when $v \leq 0.5$) correspond to the optimization iterations, $m=1, 224, 229$, and 500 , respectively. The sharpness parameter, β , is doubled at iterations $m=61, 121, 181, 241, 301$, and 361 as indicated by the black circles.

B.3. Convergence histories

As shown in Fig. B.9, we use Dsg. 8 as a representative example to show the histories of the objective (J) and constraint (g) functions. It can be observed that both the objective and constraint functions can converge in the end based on the correct sensitivity analysis in Appendix B.1. The jumps in the history of the objective function result from the updates of the sharpness parameter, β , in the Heaviside projection. Also, the fracture is naturally sensitive to the slight change in the topology, which can further promote jumps in the histories (e.g., from iterations $m=224$ to 229).

Appendix C. Numerical verification of meshes used in topology optimization

C.1. Verification of the voxel-based mesh

In this appendix, we take the Dsg. 2 as an example to show the comparison of crack paths and force–displacement curves predicted by the voxel-based mesh (fixed-grid method) (da Silva et al., 2019) in density-based topology optimization and the body-fitted mesh commonly used to manufacture designs. As for the body-fitted mesh, we use an unstructured mesh and 61,210 linear quadrilateral finite elements of size $h = \epsilon/3 = 0.05$ mm. It can be observed from Fig. C.10 that the designs of voxel-based and body-fitted meshes result in similar crack paths, and the corresponding force–displacement curves are also close to each other. The small discrepancies in force–displacement curves are due to the difference in element shapes in different meshes, and crack evolution is a local behavior sensitive to geometries. Therefore, it is reasonable to utilize the voxel-based mesh in density-based topology optimization to optimize fracture properties.

C.2. Verification of the symmetric mesh

It should be noted that, while topology optimization generally favors design symmetry, the symmetry of a FE discretization of space to carry out the pertinent calculations could have an impact on the results that are generated for fracture behaviors. To gain insight into this issue, we provide a few preliminary results. As a representative case, Fig. C.11 compares the results obtained for Dsg. 11 when generated with a symmetric mesh and an asymmetric mesh. Both results are seen to exhibit similar two stages of fracture (at the outer and inner rings, consecutively). In the result generated with the asymmetric mesh, cracks appear at the top and bottom parts of the design. By plotting the principal stress (σ_1) at critical loading steps, $u = 0.15$ and 0.16 mm in Fig. C.11(b), we observe the stress redistribution process between the two consecutive fracture stages. Immediately after the first fracture stage (from $u = 0.15$ to 0.16 mm), the principal stress is released at the left and right of the outer ring and is redistributed to the inner ring, leading to the second stage of fracture at the top and bottom parts. We also observe that cracks appear earlier than in the result generated with the symmetric mesh, and the total work required to lead to the complete failure of the structure with the asymmetric discretization is also smaller. At any rate, both force–displacement curves show similar trends (two stages of cracks) and exhibit crack displacements ($u_c = 0.17$ and 0.15 mm for the symmetric and asymmetric meshes, respectively) greater than or equal to the prescribed value ($u_n = 0.15$ mm).

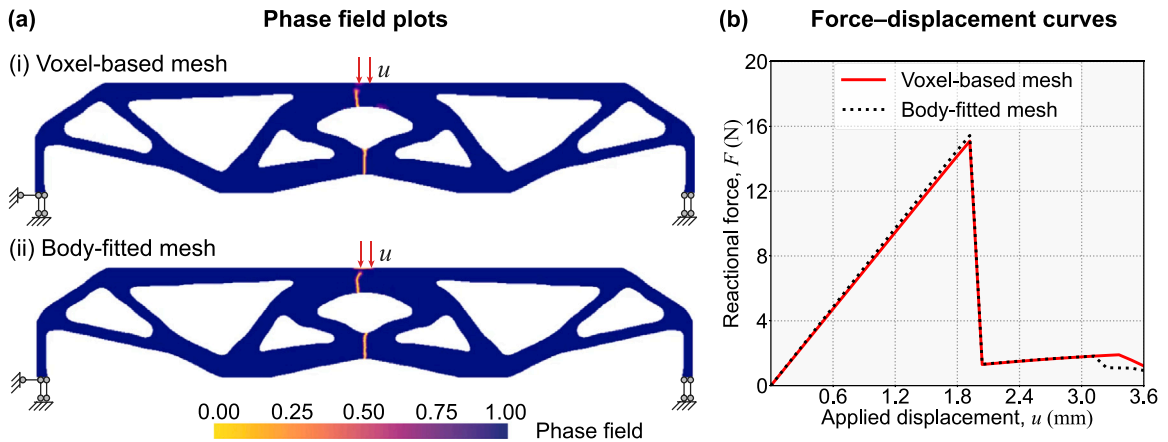


Fig. C.10. Comparison of the voxel-based mesh in density-based topology optimization and the body-fitted mesh commonly used to manufacture designs. (a) Phase field plots representing crack evolution. (b) Comparison of force–displacement curves.

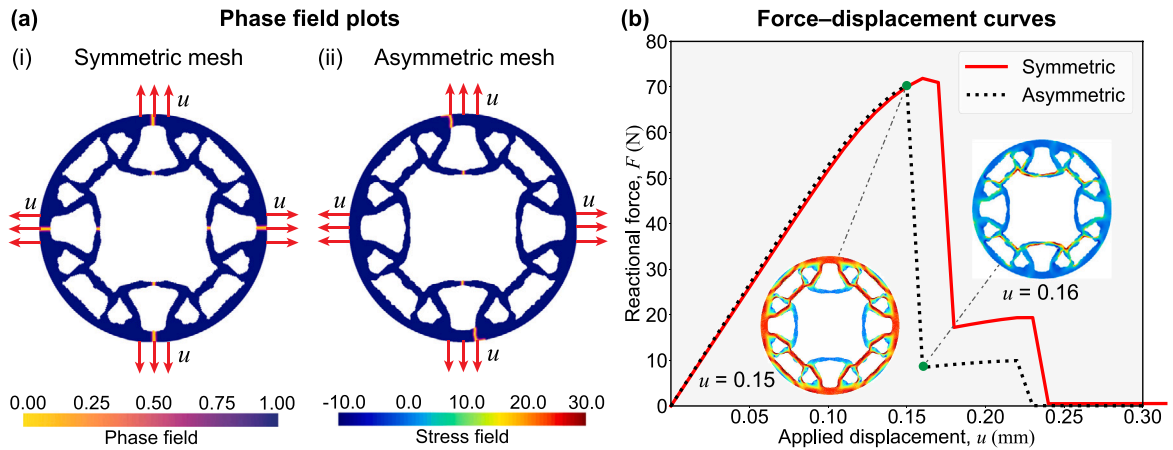


Fig. C.11. Comparison of the structural behaviors of using symmetric and asymmetric meshes of Dsg. 11. (a) Phase field plots representing crack evolution for (i) symmetric mesh and (ii) asymmetric mesh. (b) Comparison of force–displacement curves. Two insets show the principal stress, σ_1 (in MPa), of the asymmetric mesh at critical loading steps, $u = 0.15$ and 0.16 mm, respectively, where $\sigma_1 > 30$ MPa is denoted as 30 MPa and $\sigma_1 < -10$ MPa is denoted as -10 MPa for better visualization.

References

Allaire, G., 2002. *Shape Optimization By the Homogenization Method*. Springer Science & Business Media.

Bendsoe, M.P., Kikuchi, N., 1988. Generating optimal topologies in structural design using a homogenization method. *Comput. Methods Appl. Mech. Engrg.* 71 (2), 197–224.

Bendsoe, M.P., Sigmund, O., 1999. Material interpolation schemes in topology optimization. *Arch. Appl. Mech.* 69 (9), 635–654.

Bendsoe, M.P., Sigmund, O., 2003. *Topology Optimization: Theory, Methods, and Applications*. Springer Science & Business Media.

Bourdin, B., 2001. Filters in topology optimization. *Internat. J. Numer. Methods Engrg.* 50 (9), 2143–2158.

Bourdin, B., Francfort, G., Marigo, J.-J., 2000. Numerical experiments in revisited brittle fracture. *J. Mech. Phys. Solids* 48 (4), 797–826.

Bower, A., Ortiz, M., 1991. A 3-dimensional analysis of crack trapping and bridging by tough particles. *J. Mech. Phys. Solids* 39, 815–858.

Brodnik, N.R., Brach, S., Long, C.M., Ravichandran, G., Bourdin, B., Faber, K.T., Bhattacharya, K., 2021. Fracture diodes: Directional asymmetry of fracture toughness. *Phys. Rev. Lett.* 126 (2), 025503.

Cauchy, A.L., 1823. *Recherches sur l'Équilibre et le Mouvement Intérieur des Corps Solides Oufuides, Élastiquesounonélastiques*. pp. 300–304.

Chen, Y.L., Liu, B., He, X.Q., Huang, Y., Hwang, K.C., 2010. Failure analysis and the optimal toughness design of carbon nanotube-reinforced composites. *Compos. Sci. Technol.* 70 (9), 1360–1367.

Da, D., Chan, Y.-C., Wang, L., Chen, W., 2022. Data-driven and topological design of structural metamaterials for fracture resistance. *Extreme Mech. Lett.* 50, 101528.

Da, D., Chen, W., 2022. Simple strategy towards tailoring fracture properties of brittle architected materials. *Internat. J. Numer. Methods Engrg.* 124 (2).

Da, D., Qian, X., 2020. Fracture resistance design through biomimicry and topology optimization. *Extreme Mech. Lett.* 40, 100890.

Da, D., Yvonne, J., 2020. Topology optimization for maximizing the fracture resistance of periodic quasi-brittle composites structures. *Materials* 13 (15), 3279.

Da, D., Yvonne, J., Xia, L., Li, G., 2018. Topology optimization of particle-matrix composites for optimal fracture resistance taking into account interfacial damage. *Internat. J. Numer. Methods Engrg.* 115 (5), 604–626.

- da Silva, G.A., Beck, A.T., Sigmund, O., 2019. Stress-constrained topology optimization considering uniform manufacturing uncertainties. *Comput. Methods Appl. Mech. Engrg.* 344, 512–537.
- Desai, J., Allaire, G., Jouve, F., 2022. Topology optimization of structures undergoing brittle fracture. *J. Comput. Phys.* 5, 111048.
- Drucker, D.C., Prager, W., 1952. Soil mechanics and plastic analysis for limit design. *Quart. Appl. Math.* 10, 157–165.
- Francfort, G.A., Marigo, J.-J., 1998. Revisiting brittle fracture as an energy minimization problem. *J. Mech. Phys. Solids* 46 (8), 1319–1342.
- Gao, H., Rice, J., 1989. A first-order perturbation analysis of crack trapping by arrays of obstacles. *J. Appl. Mech.* 56, 828–836.
- Griffith, A.A., 1921. The phenomena of rupture and flow in solids. *Philos. Trans. R. Soc. Lond.* 221, 163–198.
- Huang, Y., Kinloch, A.J., 1992. The toughness of epoxy polymers containing microvoids. *Polymer* 33, 1330–1332.
- Jia, Y., Wang, H.-L., Liu, B., Huang, Y., Gao, H., 2020. Intrinsic-to-extrinsic transition in fracture toughness through structural design: A lesson from nature. *Extreme Mech. Lett.* 37, 100685.
- Kumar, A., Bourdin, B., Francfort, G.A., Lopez-Pamies, O., 2020. Revisiting nucleation in the phase-field approach to brittle fracture. *J. Mech. Phys. Solids* 142, 104027.
- Kumar, A., Francfort, G.A., Lopez-Pamies, O., 2018a. Fracture and healing of elastomers: A phase-transition theory and numerical implementation. *J. Mech. Phys. Solids* 112, 523–551.
- Kumar, A., Lopez-Pamies, O., 2020. The phase-field approach to self-healable fracture of elastomers: A model accounting for fracture nucleation at large, with application to a class of conspicuous experiments. *Theor. Appl. Fract. Mech.* 107, 102550.
- Kumar, A., Lopez-Pamies, O., 2021. The poker-chip experiments of Gent and Lindley (1959) explained. *J. Mech. Phys. Solids* 150, 104359.
- Kumar, A., Ravi-Chandar, K., Lopez-Pamies, O., 2018b. The configurational-forces view of fracture and healing in elastomers as a phase transition. *Int. J. Fract.* 213, 1–16.
- Kumar, A., Ravi-Chandar, K., Lopez-Pamies, O., 2022. The revisited phase-field approach to brittle fracture: Application to indentation and notch problems. *Int. J. Fract.* 236, 82–100.
- Li, W., Wang, F., Sigmund, O., Zhang, X.S., 2022. Digital synthesis of free-form multimaterial structures for realization of arbitrary programmed mechanical responses. *Proc. Natl. Acad. Sci.* 119 (10), e2120563119.
- Li, P., Wu, Y., Yvonnet, J., 2021. A SIMP-Phase field topology optimization framework to maximize quasi-brittle fracture resistance of 2D and 3D composites. *Theor. Appl. Fract. Mech.* 102919.
- Love, A.E.H., 1906. *A Treatise on the Mathematical Theory of Elasticity*. Cambridge University Press, Cambridge.
- Michel, J.C., Suquet, P., 2022. Merits and limits of a variational definition of the effective toughness of heterogeneous materials. *J. Mech. Phys. Solids* 164, 104889.
- Miehe, C., Welschinger, F., Hofacker, M., 2010. Thermodynamically consistent phase-field models of fracture: Variational principles and multi-field FE implementations. *Internat. J. Numer. Methods Engrg.* 83, 1273–1311.
- Mirkhalaf, M., Zhou, T., Barthelat, F., 2018. Simultaneous improvements of strength and toughness in topologically interlocked ceramics. *Proc. Natl. Acad. Sci.* 115 (37), 9128–9133.
- Munz, D., Fett, T., 1999. *Ceramics: Mechanical Properties, Failure Behaviour, Materials Selection*. Springer.
- Ritchie, R.O., 2021. Toughening materials: Enhancing resistance to fracture. *Phil. Trans. R. Soc. A* 379 (2203), 20200437.
- Russ, J.B., Waisman, H., 2019. Topology optimization for brittle fracture resistance. *Comput. Methods Appl. Mech. Engrg.* 347, 238–263.
- Russ, J.B., Waisman, H., 2020. A novel topology optimization formulation for enhancing fracture resistance with a single quasi-brittle material. *Internat. J. Numer. Methods Engrg.* 121 (13), 2827–2856.
- Scroggs, M.W., Dokken, J.S., Richardson, C.N., Wells, G.N., 2022. Construction of Arbitrary order finite element degree-of-freedom maps on polygonal and polyhedral cell meshes. *ACM Trans. Math. Software* 48 (2), 18:1–18:23.
- Svanberg, K., 1987. The method of moving asymptotes—a new method for structural optimization. *Internat. J. Numer. Methods Engrg.* 24 (2), 359–373.
- Tanné, E., Li, T., Bourdin, B., Marigo, J.-J., Maurini, C., 2018. Crack nucleation in variational phase-field models of brittle fracture. *J. Mech. Phys. Solids* 110, 80–99.
- Wang, C., Zhao, Z., Zhou, M., Sigmund, O., Zhang, X.S., 2021. A comprehensive review of educational articles on structural and multidisciplinary optimization. *Struct. Multidiscip. Optim.*
- Wu, C., Fang, J., Zhou, S., Zhang, Z., Sun, G., Steven, G.P., Li, Q., 2020. Level-set topology optimization for maximizing fracture resistance of brittle materials using phase-field fracture model. *Internat. J. Numer. Methods Engrg.* 121 (13), 2929–2945.
- Wu, C., Fang, J., Zhou, S., Zhang, Z., Sun, G., Steven, G.P., Li, Q., 2021. A path-dependent level set topology optimization with fracture criterion. *Comput. Struct.* 249, 106515.
- Wu, Y., Yvonnet, J., Li, P., He, Z.-C., 2022. Topology optimization for enhanced dynamic fracture resistance of structures. *Comput. Methods Appl. Mech. Engrg.* 394, 114846.
- Xia, L., Da, D., Yvonnet, J., 2018. Topology optimization for maximizing the fracture resistance of quasi-brittle composites. *Comput. Methods Appl. Mech. Engrg.* 332, 234–254.
- Zhang, J., van Keulen, F., Aragón, A.M., 2022. On tailoring fracture resistance of brittle structures: A level set interface-enriched topology optimization approach. *Comput. Methods Appl. Mech. Engrg.* 388, 114189.
- Zhao, Z., Zhang, X.S., 2021a. Additive manufacturing of topology-optimized graded porous structures: An experimental study. *JOM* 73 (7), 2022–2030.
- Zhao, Z., Zhang, X.S., 2021b. Design of graded porous bone-like structures via a multi-material topology optimization approach. *Struct. Multidiscip. Optim.* 64 (2), 677–698.